MASTERARBEIT / MASTER'S THESIS

Titel der Masterarbeit / Title of the Master's Thesis

Characterisation of Fine Mesh Photomultiplier Tubes for the ALICE Fast Interaction Trigger

verfasst von / submitted by

Sigrid Scherl, BSc

angestrebter akademischer Grad / in partial fulfilment of the requirements for the degree of

Master of Science (MSc)

Wien, 2020 / Vienna, 2020

Studienkennzahl lt. Studienblatt / degree programme code as it appears on the student record sheet:	A 066 876
Studienrichtung lt. Studienblatt / degree programme as it appears on the student record sheet:	Masterstudium Physik
Betreut von / Supervisor:	Priv.-Doz. Dr. Johann Zmeskal
Mitbetreut von / Co-Supervisor:	

Abstract

Shortly after the big bang strongly interacting matter existed as Quark-Gluon Plasma (QGP). As QGP can no longer be found in our universe today it is of high interest to generate and study this hot and dense state of matter in the laboratory, through experiments colliding heavy ions. One of those experiments is ALICE, located at the LHC at CERN in Switzerland, which studies QGP in lead ion collisions.

As the LHC is being upgraded to work at higher luminosity and performance, the ALICE experiment has to be adapted as well. For that, a new trigger system is installed in ALICE, the Fast Interaction Trigger (FIT), which serves as a forward trigger as well as a luminometer. FIT combines and replaces the three previous detectors T0, V0, and FMD by the new and enhanced T0+ and V0+.

The new V0+ consists of a segmented scintillator ring and covers a larger area than the previous V0. The scintillation light is read out by fine mesh PMTs, placed around the scintillator ring, which are connected to the scintillator segments via optical fibres.

In order to ensure optimal performance, the PMTs have to be characterised previous to their installation in the V0+ module. For that they undergo thorough testing, which includes measurements of their anode pulse rise time, gain, electron transit time, transit time spread, pulse linearity, anode uniformity, and stability over time. The evaluation of this characterisation shows that the PMTs all perform as expected and are thus ready for their installation in the V0+ module, which has already begun.

Zusammenfassung

Kurz nach dem Urknall existierte Materie, die der starken Wechselwirkung unterliegt, als Quark-Gluon-Plasma (QGP). Da QGP im heutigen Universum nicht mehr existiert, ist es von großem Interesse diese heiße und dichte Form der Materie im Labor durch Experimente mit Kollisionen von Schwerionen zu erzeugen. Eines dieser Experimente ist ALICE, welches sich am LHC am CERN in der Schweiz befindet und QGP in Kollisionen von Blei-Ionen studiert.

Da der LHC aufgerüstet wird, um bei höherer Luminosität und Leistung zu arbeiten, muss ALICE ebenfalls angepasst werden. Dafür wird ein neues Triggersystem, der Fast Interaction Trigger (FIT), in ALICE installiert. Dieser fungiert sowohl als Vorwärtstrigger als auch als Luminometer. FIT kombiniert und ersetzt die drei vorherigen Detektoren T0, V0 und FMD durch die neuen und verbesserten T0+ und V0+.

Der neue V0+ besteht aus einem segmentierten Szintillator-Ring und deckt eine größere Fläche ab als der vorherige V0. Das Szintillationslicht wird von fine mesh PMTs ausgelesen, die um den Szintillator-Ring platziert sind und durch optische Fasern mit den Szintillatorsegmenten verbunden sind.

Um eine optimale Leistung zu garantieren, müssen die Charakteristiken der PMTs vor ihrer Installation im V0+ Modul genau bestimmt werden. Dafür werden sie gründlichen Tests unterzogen, welche die Messung ihrer Anodenpuls-Anstiegszeit, Verstärkung, Transitdauer der Elektronen, Verteilung der Transitdauer, Pulslinearität, Anodenuniformität und Stabilität über Zeit umfassen. Die Auswertung dieser Charakteristiken zeigt, dass sich alle PMTs wie erwartet verhalten und daher bereit für die Installation im V0+ Modul sind, welche auch bereits angefangen hat.

Acknowledgements

My thanks go first and foremost to Hannes. Thank you for giving me this project and all the opportunities it entailed. Thank you for your guidance through it, enabling me to grow in the process and fall in love with physics all over again.

I am grateful to Eberhard, for giving me a place at SMI, where I met so many wonderful people and made great memories.

My gratitude goes to Doris, Mark, Leo, and Herbert, without whom this project would not have been possible, as the setups are really their work.

Thank you to Marlene, for taking the time to show me the ropes when I first got to SMI, and for everything else as well.

Thank you to Constanze and Vici for your help with the measurements.

Generally, thank you to all my colleagues at SMI, including Alina, Amit, Andi, Barbara, and Manfred, for just a really great time.

For getting me through university, the highs and the lows, thank you especially to the WINOs and Simon.

Lastly to my family, thank you for being the most amazing people I could hope for, especially to my parents for supporting and believing in me no matter what: this is for you.

Contents

1 Introduction

In the beginning of the universe, strongly interacting matter existed as Quark-Gluon Plasma (QGP). As the universe started to expand, it also cooled down and the quarks and gluons, like other particles, formed bonds, and eventually came to exist in their current state. The QGP is therefore no longer present in our universe, which makes it all the more mysterious and interesting, as many questions on its composition and characteristics remain. To be able to perform research on it, QGP is generated in the laboratory. This is done through experiments colliding heavy ions [1].

One of the experiments searching for QGP in heavy ion collisions is the ALICE experiment, which is located at the Large Hadron Collider (LHC) at the European Organisation for Nuclear Research, CERN (the acronym originating from the French *Conseil Européen pour la Recherche Nucléaire* [2]). A schematic overview over the LHC and the four big experiments located there is shown in figure 1.

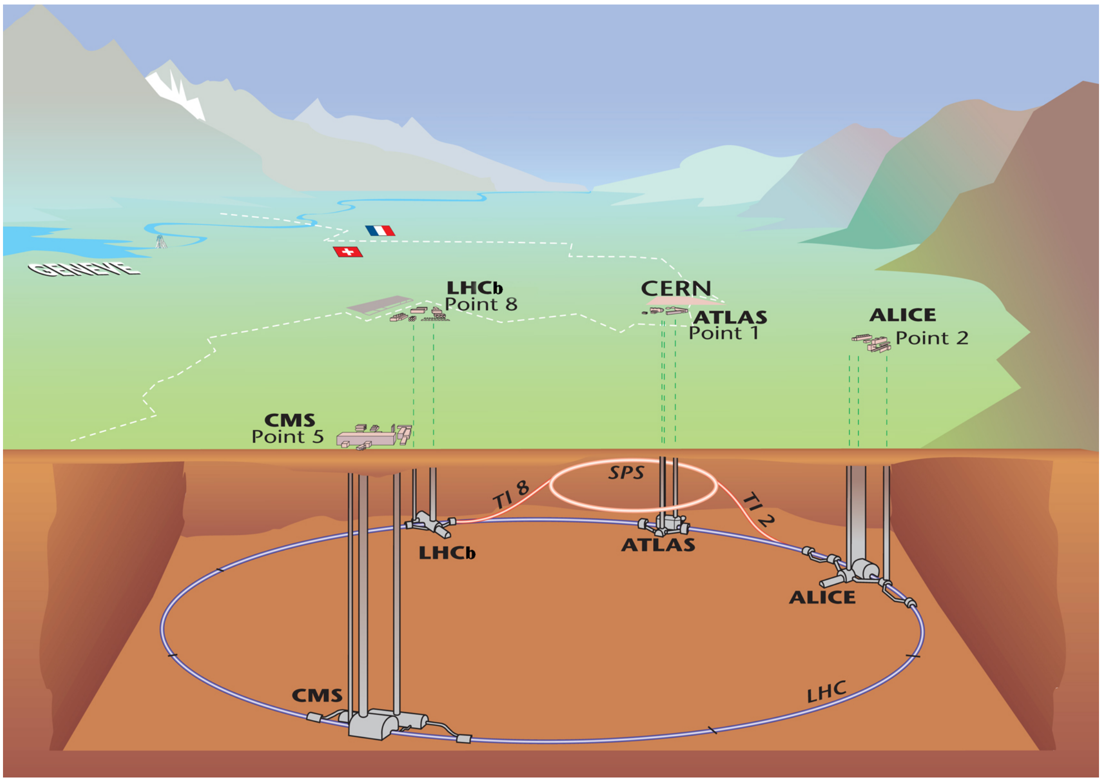

Figure 1: A schematic view of the Large Hadron Collider and the four big experiments located there: ALICE, ATLAS, CMS, and LHCb. *Picture courtesy of CERN* [3].

As the LHC is being upgraded to work at higher luminosity and performance, the ALICE experiment has to be adapted as well. For that, a new trigger system is installed in ALICE, the Fast Interaction Trigger (FIT), which serves as a forward trigger as well as a luminometer. FIT combines and replaces the three previous detectors T0, V0, and FMD by the new and enhanced T0+ and V0+. The new V0+ consists of a segmented scintillator ring and covers a larger area than the previous V0. The scintillation light is read out by fine mesh photomultiplier tubes (PMTs), placed around the scintillator ring, which are connected to the scintillator segments via fibres [4].

In order to ensure optimal performance, the PMTs have to be characterised previous to their installation in the V0+ module. For that they undergo thorough testing in three different setups, designed specifically for the measurement of their anode pulse rise time, gain, electron transit time and transit time spread, pulse linearity, anode uniformity, and stability over time.

The construction of these three setups and the measurement of the PMTs was done predominantly at the Stefan Meyer Institute (SMI) in Vienna. While the first PMTs where then already being installed in the V0+ module at CERN, the testing setups were disassembled at SMI and reassembled in a lab at the CERN site for the measurement of the last PMTs.

The description and evaluation of this characterisation of the fine mesh PMTs for the V0+ is the topic of this thesis.

2 The ALICE Experiment

2.1 Physics Motivation

This section is based on the introduction in [1].

In the early universe, at the age of 10^{-15} to 10^{-2} s [5], strongly interacting matter existed in a very hot and dense state. Quarks and gluons, which are now confined into hadrons, were not bound, but existed in a deconfined state, called Quark-Gluon Plasma. This matter, therefore, had very different properties to the hadronic matter observed in the universe today. To be able to study QGP now, it has to be created in the laboratory via collisions of heavy ions. There, heavy ions are brought to ultra-relativistic energies, bringing matter to temperatures and densities high enough to create QGP for a tiny moment, which is sufficient to collect data on this fundamental state of matter.

Although the theory of the strong force is well described by Quantum Chromodynamics (QCD), as stated in [6], questions still remain. Moving from hadronic matter to QGP, matter undergoes the deconfinement phase transition as well as the chiral phase transition. The deconfinement phase transition occurs at high temperatures, when the hadrons melt into their constituents, namely quarks and gluons, which then exist as QGP. The chiral phase transition is connected to the generation of hadronic masses, where the underlying condensates melt, reducing the quark masses to their bare values. These phase transitions are predicted to occur at different critical temperatures. Further, the transition between hadronic matter and QGP is presumed to occur over a broad range of temperature instead of having a sudden transition.

Whereas it has long been believed that QGP is a weakly interacting gas of quarks and gluons, where particles traverse long distances before interacting with each other, heavy-ion experiments have shown that QGP is instead very dense, its constituents interacting a lot while travelling through it. One of these experiments is A Large Ion Collider Experiment, short ALICE. It is one of the four major experiments located at the LHC at CERN. ALICE studies the properties of QGP in collisions of lead ions. Next to the high statistics Pb-Pb collisions, precision measurements with p-Pb and p-p collisions are used as a reference in ALICE. The experiment's aim is to verify the predictions made by lattice-QCD calculations and study the properties of QGP, so as to provide a better understanding of this fundamental state of matter. This includes for example the study of the phase transition between hadronic matter and QGP, including the determination of the critical temperature at which these transitions happen.

2.2 The Detector

As explained in [5], the ALICE experiment is designed to handle particle densities connected to Pb-Pb collisions at the LHC. As shown in figure 3 it is made up of various detectors, which can be divided into three groups.

The first type are the central barrel detectors which are situated inside the L3 solenoid with a magnetic field of 0.5 T and consist of the following detectors. The Inner Tracking system (ITS) is the innermost detector, which serves as a tracker of charged particles and is shown in more detail in figure 2. It is composed of two layers of Silicon Pixel Detectors (SPD), two layers of Silicon Drift Detectors (SDD), and two layers of Silicon Strip Detectors (SSD). The Time Projection Chamber (TPC) is also used for charged-particle tracking and additionally identifies charged particles by measuring the specific ionisation energy loss. The Transition Radiation Detector (TRD), comprising six layers of Multi-wire Proportional Chambers (MWPC), performs charged particle tracking and electron identification. The Time of Flight (TOF) detector carries out particle identification at intermediate momenta. The outermost central barrel detectors are the two electromagnetic calorimeters, the Photon Spectrometer (PHOS) and the Electromagnetic Calorimeter (EMCal), and the High Momentum Particle Identification Detector (HMPID), which is a ring-imaging Cherenkov detector.

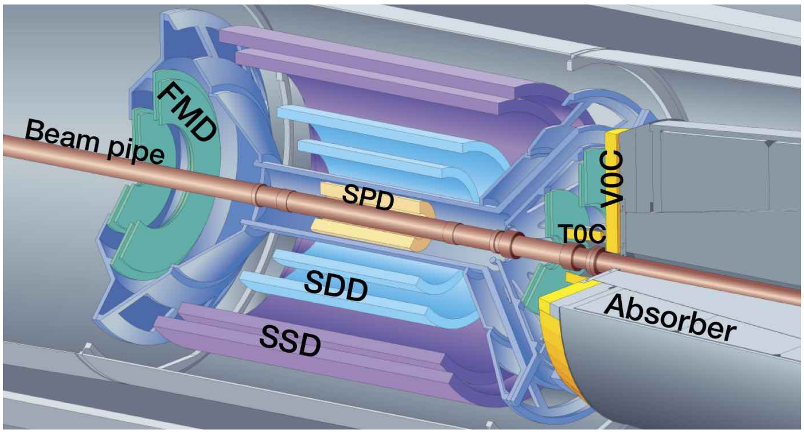

Figure 2: A schematic view of the Inner Tracking System (ITS) which belongs to the central barrel detectors of the ALICE experiment. It consists of SPDs, SDDs, and SSDs. Also pictured are parts of the T0 and V0 detectors, as well as the FMD, which are forward detectors. *Picture courtesy of CERN.*

The second type of detectors making up ALICE are the forward detectors. The Photon Multiplicity Detector (PMD) and the Forward Multiplicity Detector (FMD) cover about the same spatial region, where the PMD measures photons and the FMD charged particles. The T0 is a quartz Cherenkov detector and delivers time and spatial information on the interaction, while the V0 is a plastic scintillator detector used for triggering by the measurement of charged particles. The T0 and V0 are both made up of two parts (A and C) located on either side of the interaction point (IP). The V0 additionally measures centrality which is also done by the Zero Degree Calorimeters (ZDC), made up of two tungsten-quartz neutron (ZN) and two brass-quartz proton (ZP) calorimeters. As stated in [7] the two ZDCs, each consisting of one ZP and one ZN, are placed at a distance of 115 m on either side of the IP, close to the beam pipe, and measure the energy of spectator nucleons.

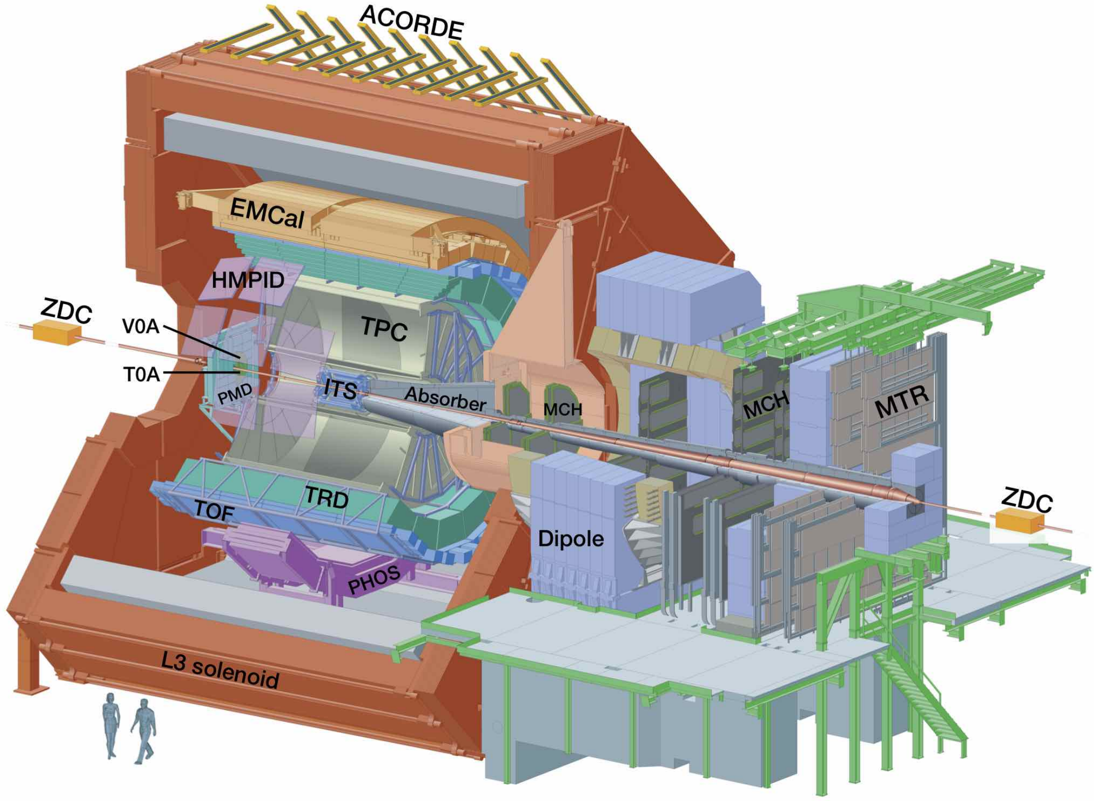

Figure 3: A schematic view of the ALICE experiment at CERN. Its three groups of detectors are the central barrel detectors (ITS, TPC, TRD, TOF, PHOS, EMCal, HMPID), the forward detectors (PMD, FMD, T0, V0, ZDC), and the muon spectrometer (MCH, MTR). They are encased in the L3 solenoid magnet, on which the cosmic-ray trigger ACORDE is placed. *Picture courtesy of CERN.*

The third detector type used in ALICE is the muon spectrometer. It monitors muons and mesons. It is composed of the Muon Chambers (MCH) and the Muon Trigger (MTR). Additionally, the cosmic-ray trigger detector ACORDE is placed on the outside of the magnet. This and further information on the ALICE detectors can be found in [5].

2.3 The Fast Interaction Trigger

During the Long Shutdown 2 (LS2), scheduled from 2019 to 2021 [8], the LHC is being upgraded to increase the luminosity and the collision rate. To profit from this increase in performance the ALICE detector is upgraded as well. Part of this upgrade is the installation of a new trigger system, the Fast Interaction Trigger (FIT). It is shown schematically in figure 4, which also indicates its size and pseudorapidity η, which describes the angle between a particle's momentum and the beam axis ([9], *page 24*). FIT combines the three forward detectors

V0, T0, and FMD to a single detector, which serves as the main forward trigger and luminometer. FIT will determine the event multiplicity, centrality, reaction plane, and time of collisions. It consists of two different parts, the V0+ and the T0+, which is again made up of two parts, the T0A+ and T0C+ (see [4], [10]).

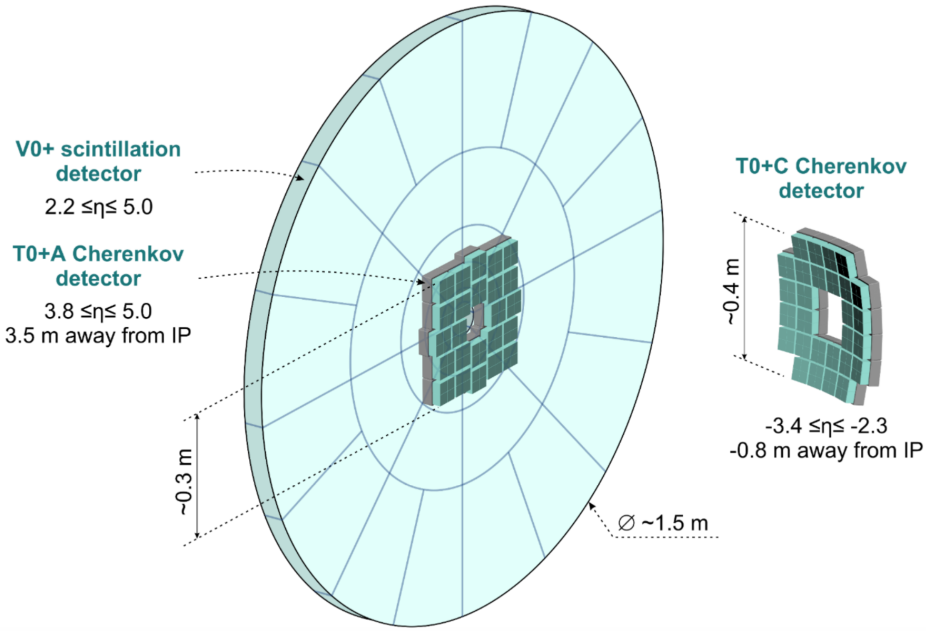

Figure 4: A schematic drawing of the Fast Interaction Trigger (FIT), consisting of the scintillation detector V0+, and the Cherenkov detectors T0A+ and T0C+. The size and pseudorapidity η of the modules are also shown. *Taken from [4].*

2.3.1 The T0+ detector

The T0+ contains two parts, the T0A+ and the T0C+, which can be seen in figure 4. T0A+ and T0C+ are both arrays of Cherenkov quartz radiators, which are connected to microchannel plate photomultiplier tubes (MCP-PMTs). They are both placed around the beam pipe and close to the interaction point (IP). The T0A+ is located where the T0A was before (see figure 3), in a distance of 3.2 m from the IP. It consists of 24 modules, each module encompassing a 2 cm thick quartz radiator (which is divided into four sections) coupled to a MCP-PMT. The T0C+ is located where the T0C was before (see figure 2). It is positioned 82 cm away from the IP, on the other side than the T0A+, and is comprised of 28 modules.

2.3.2 The V0+ detector

The V0+ is placed around the beam pipe, replacing the V0A (see figure 3), in close proximity to the T0A+. Due to spatial restrictions the V0+ is only on one side of the IP, thus there is no A and C part like for the V0 or the T0+. Instead, however, the active area of the V0+ is more than three times larger than that of the V0.

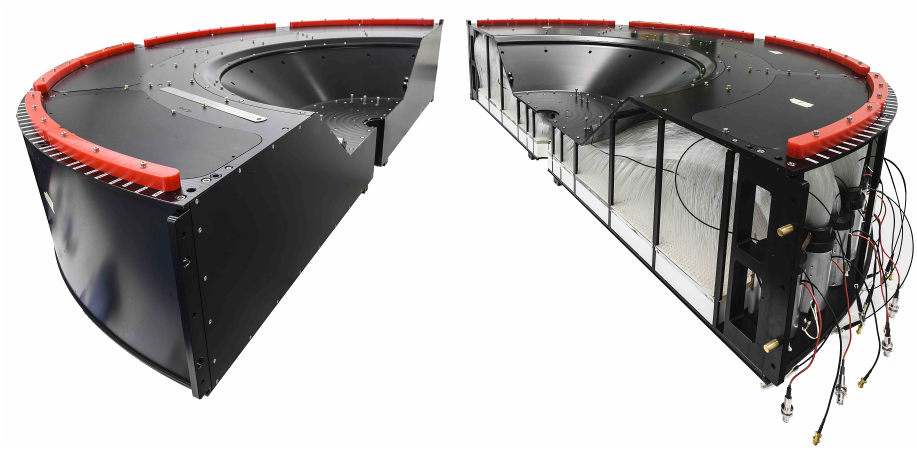

Figure 5: The V0+ detector. The left half is fully encased while the right half is shown without the side panels of the casing, enabling the view of the scintillator segments, fibres, and mounted fine mesh PMTs. *Picture courtesy of W. H. Trzaska.*

The V0+ is a scintillator ring and can be seen schematically in figure 4. It has an outer diameter of 148 cm and an inner diameter of 8 cm, which is enough space for the beam pipe to go through. The scintillator ring is divided into five rings and eight 45° sectors. They are coupled to fine mesh photomultiplier tubes via clear fibres which transmit the scintillation light. For assembling purposes, the V0+ is split vertically into two halves, thus each half consists of four 45° sectors. The assembled V0+ detector can be seen in figure 5, where the left half is already fully within its casing, whereas the casing of the right half of the detector is still open. Figure 6 shows the not fully cased half of the V0+ detector more closely, displaying the scintillator segments, the fibres, and the mounted fine mesh PMTs. The working principle and characterisation of these fine mesh PMTs are described in the following chapters.

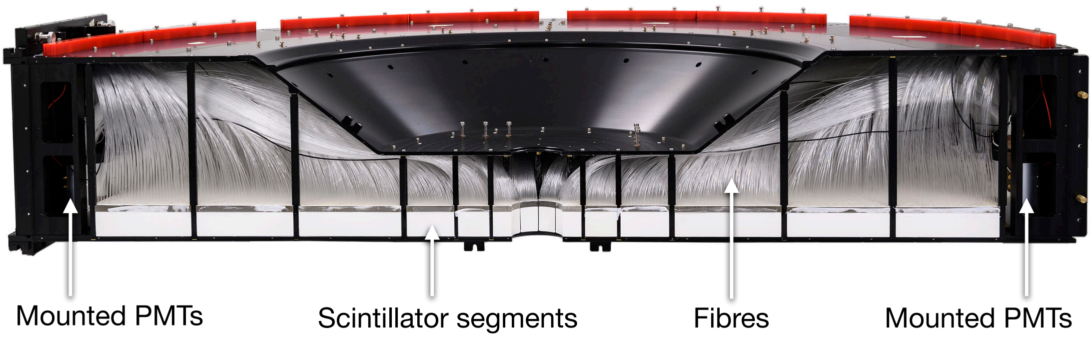

Figure 6: One half of the V0+ detector in its still open casing. *Picture courtesy of W. H. Trzaska.*

3 Photomultiplier Tubes

3.1 The Physics of Photomultiplier Tubes

A photomultiplier tube (PMT) is a detector for measuring photons and converting them into an electric current, which can be measured and is proportional to the number of incident photons. This chapter follows the description of PMTs as outlined by W. R. Leo [11], *pages 177 - 198*. When incoming photons hit the photocathode of the PMT, which is made of photosensitive material, electrons are emitted due to the photoelectric effect. These electrons, referred to as photoelectrons, then move to the first dynode due to an applied voltage. There they deposit some of their energy, causing secondary electrons to be emitted, which are then accelerated onto the next dynode, where they are multiplied again. Thus, a cascade of electrons is produced which is collected by the anode and results in a current that can be measured. A schematic drawing of a PMT and its mode of operation can be seen in figure 7.

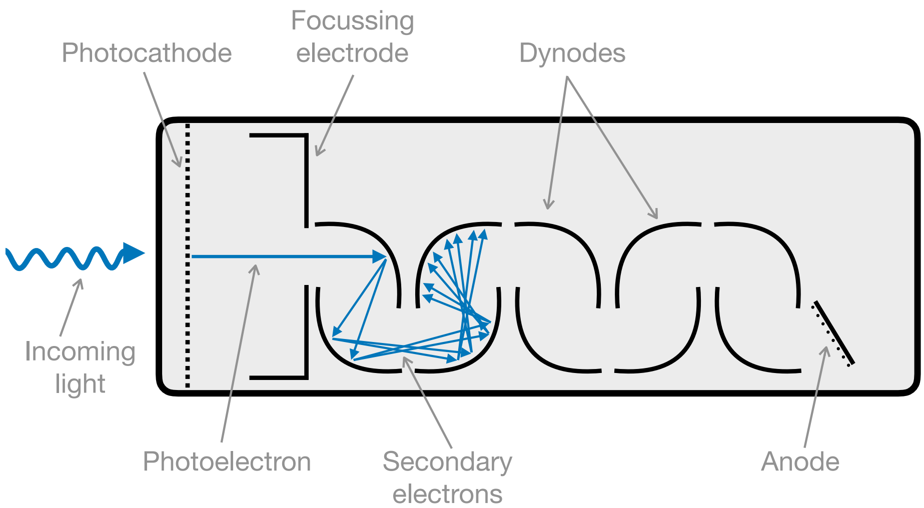

Figure 7: A schematic diagram of a photomultiplier tube.

The measured current given by a PMT depends not only on the amount of incoming light, but also on the quantum efficiency of the photocathode and the gain of the PMT. When the incident photons hit the photocathode, not every photon causes the emission of exactly one photoelectron. Instead the number of photoelectrons emitted per photon is specified by the quantum efficiency QE.

$$\mathrm{QE} = \frac{\text{number of photoelectrons released}}{\text{number of incident photons on cathode}} \tag{3.1}$$

The quantum efficiency depends on the wavelength of the incident light, as well as the material of the photocathode. Semiconductors are the most popular materials for photocathodes as they have quantum efficiencies between 10 % and 30 %, while for metals, for instance, the quantum efficiency lies under 0.1 %. As the quantum efficiency is also dependent on the wavelength, materials for the photocathode are often chosen so that the quantum efficiency peaks for light with a wavelength of about 400 nm, making them perfectly fitted for the use with scintillators.

The gain is the overall amplification of the PMT. It depends on the voltage that is applied to the PMT, as well as the number of dynodes. The total gain G of a PMT with n dynodes and an applied voltage of V is given by

$$G = \left(K \cdot \frac{V}{n}\right)^n = (K \cdot V_d)^n \tag{3.2}$$

where K is a proportionality constant and $V_d = V/n$ is the potential difference between the dynodes. Looking at the variation of the gain dG with respect to the variation of dV_d, given by

$$\frac{dG}{G} = n \cdot \frac{dV_d}{V_d} \tag{3.3}$$

clearly shows that a small change in V_d, and thus in the supply voltage V, can lead to a great change in the gain, for a large number of dynodes. Thus, a stable voltage supply is needed for a stable gain.

PMTs can be further characterised by their time resolution which is given by the variation of the electron transit time. The electron transit time is the time it takes for the electrons to pass through the PMT, meaning the time difference between the light entering the PMT and the signal output ([12], *page 192*). Variations in the transit time can occur because of the geometry of the PMT. For example, electrons being emitted near the edge of the PMT having a longer distance to travel, resulting in a greater transit time. This can be counteracted by adapting the electric field in the PMT so that the electrons near the edge are accelerated faster, compensating for the longer route. Variations can, however, also occur due to the energy of the electrons, and the direction in which they are emitted. Electrons emitted perpendicular to the photocathode and with higher energies will be quicker to reach the next dynode than the ones emitted almost parallelly to the cathode, or with lower energy. This variation is called the transit time spread.

In timing applications, it is important to know the electron transit time, as well as the rapidity of the signal. This rapidity is characterised by the rise time. This is the time it takes for the pulse to grow from 10% to 90% of the final pulse amplitude.

Looking at the generated pulse, it is also of great importance that the PMT exhibits a good linearity, so that it works over a broad range of incoming light. In order to achieve good linearity, all of the charge at a dynode must be collected by the next dynode and finally reach the anode. The difficulty here lies in the fact that a cloud of electrons, called space charge, forms around each dynode in the PMT. This space charge counteracts the electric field inside the PMT, preventing the acceleration of the electrons and thus their subsequent movement towards the anode. By applying a high enough voltage to the PMT this space charge can be collected as well, so that all the electrons reach the anode, and thus good linearity is ensured.

Loss of electrons is not only connected to the linearity, but also to the uniformity of the PMT. Charge can be lost due to the applied voltage being too low, but also when the light enters the PMT off-centre. While photons hitting the photocathode at its centre will cause the photoelectrons to be emitted at approximately a right angle, photons reaching only the outer edge of the photocathode induce the emittance of photoelectrons at an angle largely deviating from 90°. Thus, not all of the secondary electrons will make it to the anode. This lost charge consequently causes the output current to be lower than expected. The degree of reduction of output current depends on the position of the incident light, as well as on the type of the PMT (see [12]).

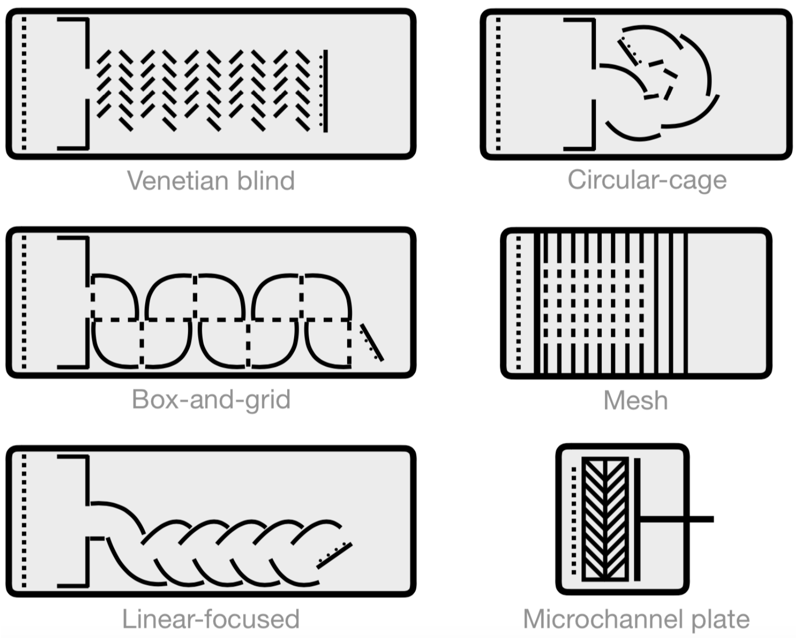

Figure 8: Schematic drawings of different PMTs, based on their type of dynodes: venetian blind type, box-and-grid type, linear-focused type, circular-cage type, mesh type, and microchannel plate type.

In addition to the photocathode material, PMTs can also be divided into different types based on their dynode structure, as described in [12]. A schematic drawing of different types of dynode structures can be seen in figure 8. The Venetian blind type, box-and-grid type, and linear-focused type are mainly used for head-on photomultiplier tubes, while the circular-cage type is used also for side-on photomultiplier tubes. The circular-cage type has a fast time response, which is also exhibited by the linear-focused type, in addition to a good time resolution and pulse linearity. The box-and-grid type, on the other hand, has a high detection efficiency and good uniformity, compared to other PMTs. While most types have problems operating in magnetic fields, there are two types of dynode structures working well in that environment. A microchannel plate (MCP) type has an excellent time resolution and a stable gain in high magnetic fields. Mesh types on the other hand have an exceptional output linearity, and especially fine mesh types have a high immunity to magnetic fields. Fine mesh PMTs are described in more detail in the following section.

3.2 The Principle of Fine Mesh Photomultiplier Tubes

While other types of photomultiplier tubes already show high variations in low magnetic fields, mesh PMTs, especially fine mesh PMTs, perform well even in high magnetic fields of over 1 T [12]. They are therefore perfectly fitted to work in high-energy physics applications where a high magnetic field is used for particle tracking, and were thus chosen for the V0+ detector inside the ALICE experiment.

As described in [12], fine mesh PMTs have dynodes consisting of mesh electrodes, which are stacked closely together. The number of dynode stages can vary for different fine-mesh PMTs. The triode type has only one dynode stage and the tetrode type has two dynode stages, while fine mesh PMTs build for high gain have 19 dynode stages. Due to the proximity and large area of the dynodes, space charge effects inside the PMT can be avoided. Thus, fine mesh PMTs exhibit excellent linearity. This dynode structure also leads to good uniformity of the PMT. A schematic drawing of a fine mesh PMT and fine mesh dynode can be seen in figure 9.

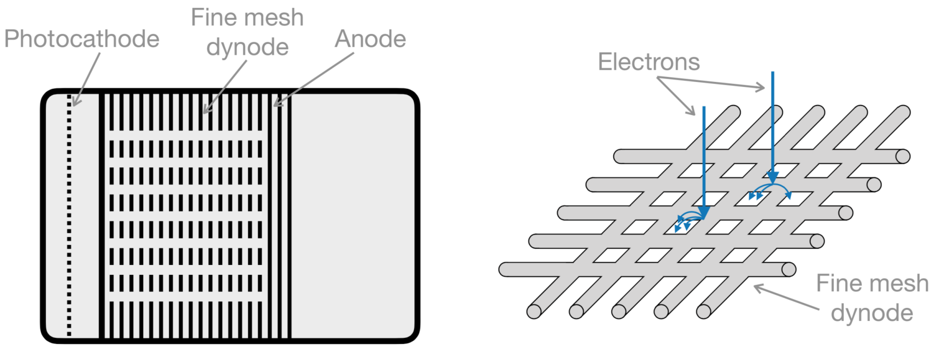

Figure 9: Schematic drawing of a fine mesh PMT (left) with a closeup of a fine mesh dynode (right).

The fine mesh PMTs chosen for the V0+ detector in the ALICE experiment are assembled fine mesh PMTs of type H6614-70 by Hamamatsu. They have a total outer diameter of 60 mm and a photocathode with a diameter of 39 mm, which is made of Bialkali [13]. Further specifications can be found in table 1. While table 2 lists the typical values of this PMT type, the exact specifications of the 54 measured PMTs, which have been determined for every single PMT via measurement, can be found in later sections.

Assembly diameter	60 mm
PMT tube diameter	51 mm
Photocathode diameter	39 mm
Peak wavelength	420 mm
Photocathode material	Bialkali
Window material	Borosilicate glass
Dynode structure	Fine mesh
Dynode stages	19

Table 1: Specifications of the fine mesh photomultiplier tube assembly H6614-70 by Hamamatsu as found in [13].

Average anode current	0.33 mA
Typical blue sensitivity index	9
Typical gain	$1.0 \cdot 10^7$
Typical rise time	2.5 ns
Typical transit time	9.5 ns
Typical transit time spread	0.44 ns
5% deviation from pulse linearity	700 mA

Table 2: Typical values at an applied voltage of 2000 V for the fine mesh photomultiplier tube assembly H6614-70 by Hamamatsu as found in [13].

A picture of two fine mesh PMTs of type H6614-70 by Hamamatsu can be seen in figure 10. They are mounted in the experimental setup 1, which is discussed in section 5.2.

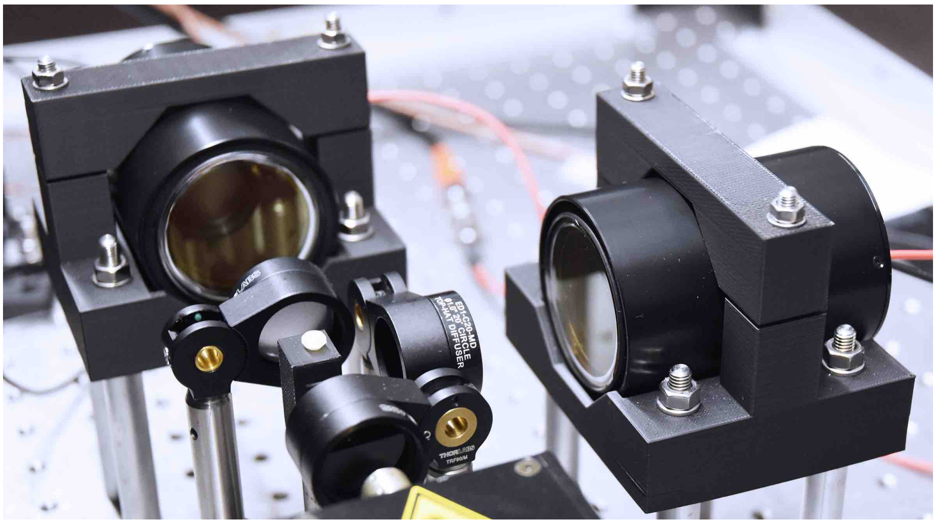

Figure 10: Two Hamamatsu H6614-70 fine mesh PMT mounted for an experimental setup. *Picture courtesy of D. Pristauz-Telsnigg.*

4 Determination of the Expected Values

As described in section 3.1, different features of a PMT need to be considered in order to characterise it. The determination of these characteristics is the aim of this work, to ensure that they operate within the expected range. Thus, the following measurements are conducted:

- Anode Pulse Rise Time
- Gain
- Electron Transit Time and Transit Time Spread
- Pulse Linearity
- Anode Uniformity
- Stability

The measurements and their results are explained in section 6. To be able to conduct and evaluate these measurements, some values of the PMTs have to be determined beforehand. These are the quantum efficiency and the expected signal amplitude for an assumed gain in dependence of the number of incident photons.

4.1 The Quantum Efficiency

As explained in section 3.1, the quantum efficiency is the number of photoelectrons being emitted by the photocathode for every incident photon. However, it is not given by Hamamatsu directly. Instead the test sheets list the blue sensitivity index for each PMT. The blue sensitivity is the cathode current divided by the incident luminous flux from a tungsten lamp at 2856 K, with a blue filter placed in front of the PMT. As the light passes through the blue filter, the blue sensitivity cannot be expressed directly in units, but instead as a unitless index [12]. The technical information [14] gives the relation between the quantum efficiency and the blue sensitivity index, which can be seen in figure 11.

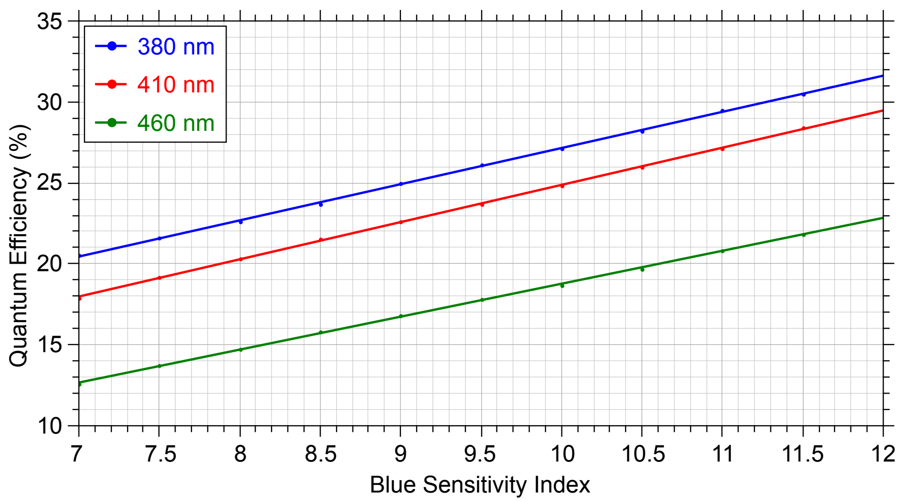

Figure 11: The quantum efficiency versus the blue sensitivity index for different wavelengths of light. *Adapted from* [14].

Using figure 11 together with the blue sensitivity index given by Hamamatsu (listed in table 3) the quantum efficiency of each PMT can be determined. The values for the quantum efficiencies are listed in table 3 for a wavelength of approximately 404 nm, which is the wavelength of the laser used for the measurements. They have an uncertainty of ±0.5. The tested PMTs are given by their serial number.

PMT Number	Blue Sensitivity Index	Quantum Efficiency (%)	PMT Number	Blue Sensitivity Index	Quantum Efficiency (%)
RA2622	10.50	26.0	RA2932	11.80	29.0
RA2632	13.30	32.5	RA2934	12.10	30.0
RA2840	11.20	28.0	RA2937	11.60	28.5
RA2843	10.20	25.5	RA2938	11.10	27.5
RA2850	11.90	29.5	RA2940	13.10	32.0
RA2880	11.70	29.0	RA2958	11.10	27.5
RA2881	10.80	27.0	RA2960	10.60	26.5
RA2884	12.30	30.5	RA2961	10.40	26.0
RA2888	10.90	27.0	RA2962	10.20	25.5
RA2889	10.10	25.0	RA2965	9.96	25.0
RA2890	11.50	28.5	RA2968	10.10	25.0
RA2891	9.78	24.5	RA2972	9.80	24.5
RA2892	10.60	26.5	RA2976	10.10	25.0
RA2903	11.90	29.5	RA2987	9.78	24.5
RA2904	12.20	30.0	RA2988	9.76	24.5
RA2908	11.60	28.5	RA2995	10.40	26.0
RA2909	11.10	27.5	RA2996	10.40	26.0
RA2910	11.30	28.0	RA3004	9.07	23.0
RA2918	11.00	27.5	RA3006	10.20	25.5
RA2922	10.20	25.5	RA3007	9.59	24.0
RA2923	10.80	27.0	RA3010	11.40	28.0
RA2924	10.30	25.5	ZU4328	11.40	28.0
RA2925	12.50	31.0	ZU4329	11.00	27.5
RA2926	11.60	28.5	ZU4330	11.30	28.0
RA2927	11.10	27.5	ZU4403	10.20	25.5
RA2928	10.30	25.5	ZU4404	10.10	25.0
RA2929	11.60	26.5	ZU4407	10.40	26.0

Table 3: The serial number, blue sensitivity index, and resulting quantum efficiency for a wavelength of 404 nm for the tested Hamamatsu fine mesh PMTs. The values for the quantum efficiency have an uncertainty of ±0.5.

4.2 The Pulse Height

Calculating the signal amplitude of a PMT, given the number of photons emitted by the laser, has to be done for each PMT separately, as the signal amplitude varies for each PMT, depending on the gain and quantum efficiency. Discussed here is a general calculation valid for every PMT. It assumes a simplified setup, shown in figure 12, as different additional parts of the final setup further modify the calculation. This simple setup consists of a Picosecond Injection Laser with a wavelength λ and pulse energy of E_{L}, a filter that reduces the number of photons corresponding to its transmission factor T_{F}, a diffuser for getting a bigger homogeneous spot size with a transmission factor T_{D}, and the corresponding photomultiplier tube with quantum efficiency QE. These four elements are present in all the actual setups described in chapter 5. A more detailed description of the equipment can be found in chapter 5.1.

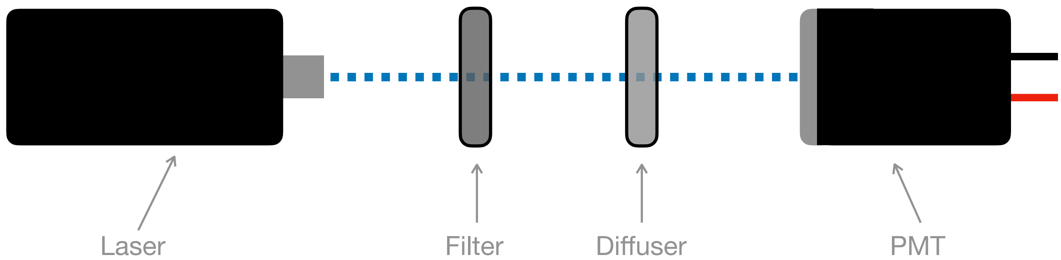

Figure 12: Simplified setup similar to the ones described in chapter 5. The photons travel from the laser through a filter and a diffuser before reaching the PMT.

Given the pulse energy E_{L} of the laser and energy E_γ of the photons the number of photons γ emitted by the laser is

$$\gamma = \frac{E_{\mathrm{L}}}{E_\gamma} \tag{4.1}$$

The number of photons is then reduced by the filter according to its transmission factor T_{F} and by the diffuser with a transmission factor T_{D} before entering the PMT. There they induce photoelectrons e_γ with a probability given by the quantum efficiency QE:

$$e_\gamma = \gamma \cdot T_{\mathrm{F}} \cdot T_{\mathrm{D}} \cdot QE \tag{4.2}$$

The photoelectrons are then multiplied by the gain G, which depends on the number of dynodes and the applied voltage. The total charge q of the resulting photoelectrons being collected by the anode is then obtain by multiplying with the elementary charge q_{e}:

$$q = e_\gamma \cdot G \cdot q_{\mathrm{e}} \tag{4.3}$$

The pulse has approximately a triangle shape. The charge q corresponds to the area of this triangle, the length of its base being the length of the pulse, t. The height of the triangle corresponds to the current i. These relations are shown graphically in figure 13.

$$q = \frac{t \cdot i}{2} \Rightarrow i = \frac{2 \cdot q}{t} \tag{4.4}$$

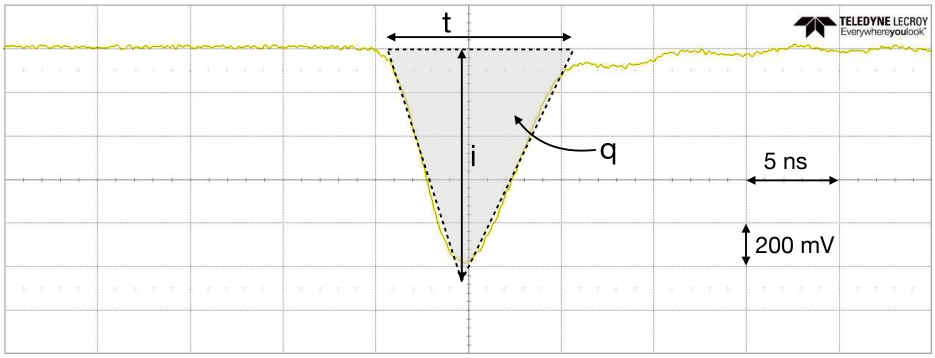

Figure 13: The measured signal of PMT RA2632 at an applied voltage of 1250 V, a frequency of 200 Hz and a laser tune value of 60%. The signal shape is roughly a triangle, whose area is half of the signal length t multiplied by the height of the triangle which corresponds to the current i.

With the current i and the resistance R the voltage U can then be calculated, which will be observed as the amplitude of the PMT signal.

$$U = R \cdot i \tag{4.5}$$

Combining all these equations leads to a single formula for the pulse height U.

$$U = \frac{E_{\mathrm{L}} \cdot QE \cdot T_{\mathrm{D}} \cdot T_{\mathrm{F}} \cdot q_{\mathrm{e}} \cdot G \cdot 2 \cdot R}{E_{\gamma} \cdot t} \tag{4.6}$$

Table 4 shows the variables from equation 4.6 with their values. QE and G are not listed as they differ for every PMT. These values for each PMT can be found it table 3 and table 9, respectively. G can also be calculated by rearranging equation 4.6 and plugging in a value for U.

Description	Variable	Value
Pulse energy of the laser	E_{L}	$2.108 \cdot 10^{8}\,\mathrm{eV}$
Photon engery of the laser	E_{γ}	$3.069\,\mathrm{eV}$
Transmission of the diffuser	T_{D}	0.90
Transmission of the filter	T_{F}	$2.416 \cdot 10^{-4}$
Electron charge	q_{e}	$1.602 \cdot 10^{-19}\,\mathrm{C}$
Resistance	R	$50\,\Omega$
Pulse length	t	$10\,\mathrm{nm}$

Table 4: The variables from equation 4.6, together with their values. The quantum efficiency QE and gain G are not listed as they vary for each PMT.

4.3 Applied Voltage vs. Gain

The expected signal height for the PMTs can be calculated straightforwardly, as shown in section 4.2. To determine the high voltage that has to be applied to a PMT to get a certain gain is, however, not as trivial. To do this, three different values of applied high voltage are plotted against the measured resulting gain for a certain PMT. By fitting an exponential curve through these points the required values can be determined for the given PMT. The plot with exponential fit for a specific PMT is shown in figure 14. The used gain values for the PMT can be found in table 9. The exponential fit has the form

$$G(HV) = p_0 + p_1 \cdot \exp\left(p_2 \cdot HV\right) \tag{4.7}$$

where $G(HV)$ is the gain as a function of the applied high voltage HV. Inversing this gives the applied voltage $HV(G)$ as a function of the gain G.

$$HV(G) = \frac{\log\left(\frac{G-p_0}{p_1}\right)}{p_2} \tag{4.8}$$

The fit gives the variables p_0, p_1, and p_2. Inserting them into equation 4.8, one can calculate the applied voltage HV that is needed for any given gain G for the PMT.

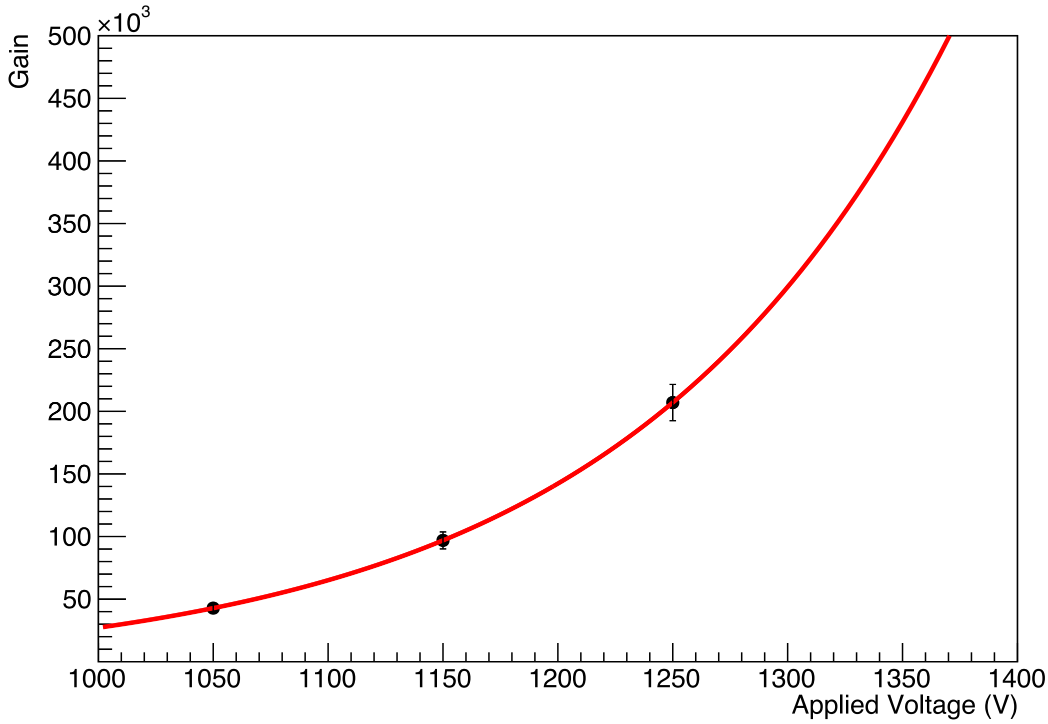

Figure 14: Exponential fit of three plotted values of the applied high voltage HV versus the gain G of PMT RA2881. The errorbars show the 7 % maximum uncertainty of the gain values.

5 Experimental Setups

For the measurement of the PMTs three different setups are needed, which are placed inside a light tight box. The first setup is for measuring two different PMTs simultaneously, as to be more time efficient, with the PMTs on fixed positions. This setup is used for the measurements of the anode pulse rise time, gain, electron transit time, transit time spread, and stability over time.

In the second setup the measured PMT is placed on a motorised positioning table and a second beamsplitter is used to create two beams of different intensity. Thus, the PMT can be moved between these two beams during the measurement. This is used for the determination of the pulse linearity.

In the third setup the PMT is fixed, but the laser light is guided through an optical fibre, which is attached to the motorised positioning table, this time with two movable axes. This way the laser beam can be moved to hit different points on the PMTs photocathode surface. This is used for the measurement of the anode uniformity.

The three different setups are described in detail in sections 5.2, 5.3, and 5.4. The principle equipment used for these setups is discussed in section 5.1.

5.1 Equipment

5.1.1 Laser

The laser used for the measurements is a Picosecond Injection Laser (PiLas) from Advanced Laser Diode Systems (A.L.S.). The pulse energy given by [15] is $E_{\mathrm{L}} = 34\,\mathrm{pJ}$ which corresponds to $E_{\mathrm{L}} = 2.108 \cdot 10^{8}\,\mathrm{eV}$. This value has an uncertainty of $3\,\%$. The specifications of the laser head are listed in table 5. Further information can be found in [16].

Average power at maximum repetition rate	P_0	$40\,\mu\mathrm{W}$
Peak radiant power	P_{p}	$1300\,\mathrm{mW}$
Pulse width	t	$28\,\mathrm{ps}$
Maximum pulse repetition rate	f	$1\,\mathrm{MHz}$
Wavelength	λ	$404\,\mathrm{nm}$

Table 5: The specifications of the laser head *PIL040*.

5.1.2 Filter

The filter that is used in all of the setups is a NE30A absorptive neutral density filter with an optical density of $OD = 3.0$ and a diameter of 25 mm by Thorlabs. As stated in [17] the optical density OD and transmission T_{F} are connected by

$$OD = \log_{10}\left(\frac{1}{T_{\mathrm{F}}}\right) \Leftrightarrow T_{\mathrm{F}} = 10^{-OD} \tag{5.1}$$

Thus, with an optical density of $OD = 3.0$ the filter has a transmission of $T_\mathrm{F} = 0.001$. However, this value also dependents on the wavelength. Thorlabs [18] specifies the transmission of the filter to be $T_\mathrm{F} = 2.416 \cdot 10^{-2}\%$ for a wavelength of 404 nm, this leads to $T_\mathrm{F} = 2.416 \cdot 10^{-4}$. This is the value that is also used in the calculations in section 4.

5.1.3 Diffuser

The diffusers that are used in all of the setups are ED1-C20-MD 20° circle tophat engineered diffusers with a diameter of 1 inch by Thorlabs. They transform the small beam spot into a beam with a larger, homogeneous area. The diffusers have a transmission efficiency of 90 %, as stated in [19], giving $T_\mathrm{D} = 0.9$ which is used in the calculations in section 4.

5.1.4 Beamsplitter

In the setups two beamsplitters are used. They split the incoming light (e.g. the laser beam) with a certain ratio into two separate beams, the transmitted beam going straight though the beamsplitter and the reflected beam exiting the beamsplitter at a 90° angle to the incoming beam. As can be seen in [20] the splitting ratio is also dependent on the wavelength of the incoming light, thus it can deviate from the given value. Thorlabs also states that some light will be absorbed by the beamsplitter coating, meaning the transmitted and reflected light do not necessarily equal the total amount of light going into the beamsplitter.

The first beamsplitter is a BS010 50:50 non-polarising beamsplitter cube with a diameter of 10 mm by Thorlabs. It is used in setup 1 and 2. [21] gives the exact splitting ratio of the beamsplitter for polarised light. However, the laser used here is unpolarised. Using the values for polarised light for a wavelength of 404 nm, together with test measurements of the beamsplitter the intensities of the outgoing beams were determined to be $I_\mathrm{t} = 47\,\%$ of the incoming beam for the transmitted beam and $I_\mathrm{r} = 43\,\%$ of the incoming beam for the reflected beam. They have a maximal uncertainty of ± 2.

The second beamsplitter is a BS049 70:30 non-polarising beamsplitter cube with a diameter of 10 mm by Thorlabs. Looking at the values for polarised light found in [22] as a reference together with measurement results, the intensity of the transmitted beam has been determined to be $I_\mathrm{t} = 62\,\%$ of the incoming beam and the intensity of the reflected beam is $I_\mathrm{r} = 28\,\%$ of the incoming beam. The values have a maximal uncertainty of ± 2.

5.1.5 Motorised positioning table

The motorised positioning table used in setup 2 and 3 to move the PMT is a Colibri-L step motor positioning table MPT17 by Gunda Electronics. The PMT is mounted on the positioning table, which is controlled via the BAC (Basic Automation Component) positioning control system, also by Gunda Electronics. The range of movement of the table is 50 mm. The movement is described and controlled in steps, where 500 steps are (2.51 ± 0.12) mm, as determined by V. Kletzl at the Stefan Meyer Institute (SMI) in Vienna. For setup 3, two such step motor positioning table units have been combined for movement along two axes.

5.2 Setup 1

Setup 1 is used for the determination of the anode pulse rise time, gain, electron transit time, transit time spread, and stability. In this setup two PMTs can be tested at the same time. To make this possible, the BS010 50:50 non-polarising beamsplitter cube is used, generating two beams of similar intensity. The beam emitted by the PiLas laser goes through the NE30A filter, where the number of photons is reduced, then through the BS010 50:50 non-polarising beamsplitter cube, where the beam is split into two separate beams with slightly less than half of the initial beam intensity. Both beams then pass an ED1-C20-MD 20° circle tophat engineered diffuser, to produce larger beam spots, and followingly enter the PMTs. This setup is shown in figure 15.

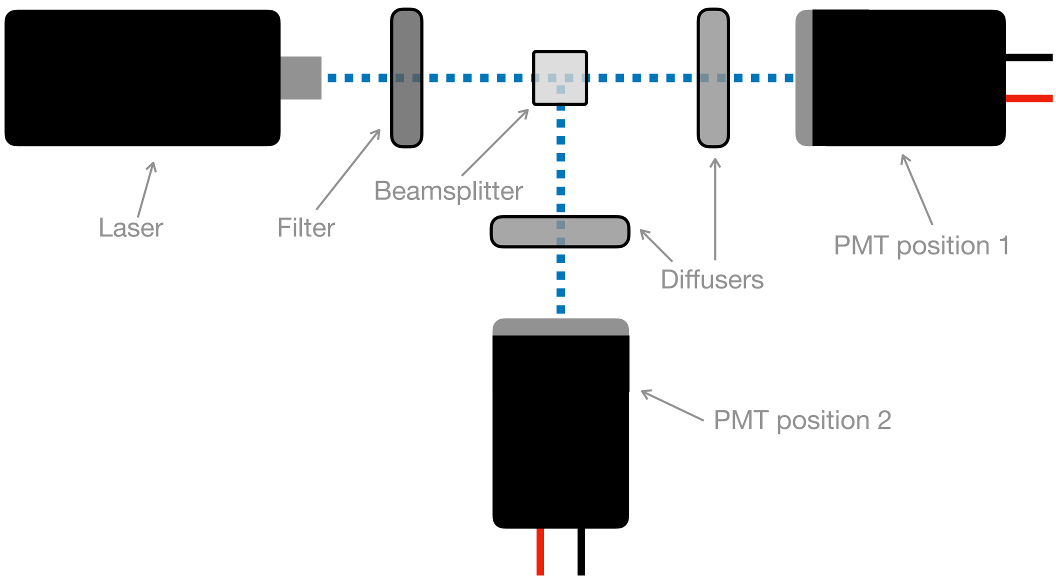

Figure 15: Setup 1 consists of a picosecond injection laser, a NE30A filter, a BS010 50:50 beamsplitter, two ED1-C20-MD 20° circle tophat engineered diffusers, and the two PMTs which are to be measured.

The reduction of the beam intensity by the beamsplitter has not yet been taken into account in equation 4.6. For this setup equation 4.6 therefore has to be expanded to include a factor I relating to the intensity of the beam exiting the beamsplitter. As already mentioned in section 5.1.4 this factor I is $I_t = 47\,\% = 0.47$ for the transmitted beam, and $I_r = 43\,\% = 0.43$ for the reflected beam. The adapted equation 4.6 for this setup therefore is

$$U = \frac{E_L \cdot QE \cdot T_D \cdot T_F \cdot I \cdot q_e \cdot G \cdot 2 \cdot R}{E_\gamma \cdot t} \tag{5.2}$$

where I is replaced by I_t for a PMT in position 1 or I_r for a PMT in position 2.

5.3 Setup 2

Setup 2 is used to determine the pulse linearity of a PMT. For this, it is necessary to measure laser pulses of two different intensities with one PMT. To generate these beams two beamsplitters with different splitting ratios are used. The PMT is fixed onto a positioning table with one motorised axis and can this way be moved between the two different beams. The setup is shown in figure 16.

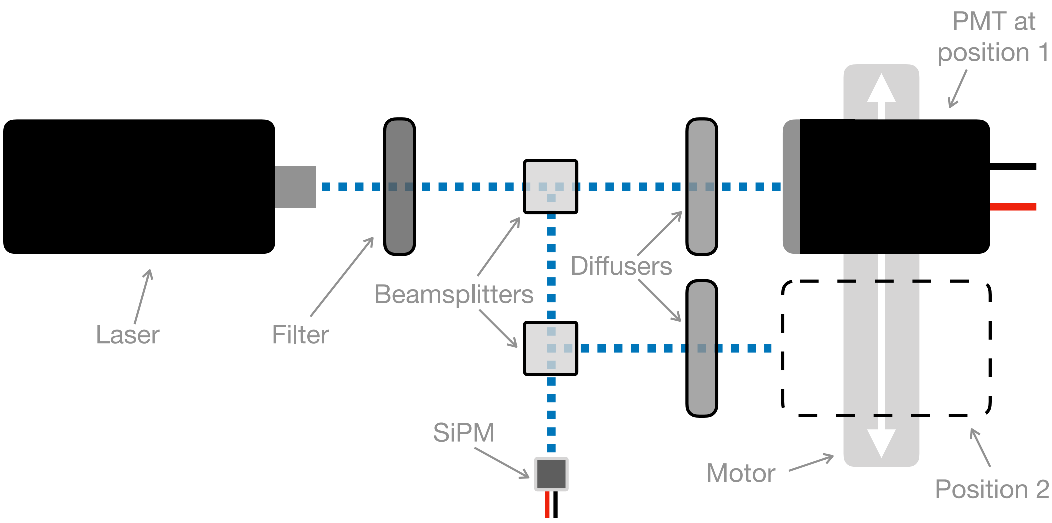

Figure 16: Setup 2 consists of a picosecond injection laser, a NE30A filter, a BS010 50:50 beamsplitter, a BS049 70:30 beamsplitter, two ED1-C20-MD 20° circle tophat engineered diffusers, a SiPM, a positioning table with one motorised axis, and the PMT which is to be measured.

The laser beam travels through a NE30A filter followed by the first beamsplitter, which is a BS010 50:50 non-polarising beamsplitter cube. There the beam is split in two, the first one going through an ED1-C20-MD 20° circle tophat engineered diffuser and exiting at the first PMT position. The second beam travels through the second beam splitter, a BS049 70:30 non-polarising beamsplitter cube, being again split into two. One of those beams goes through the other ED1-C20-MD 20° circle tophat engineered diffuser and exits at the second PMT position. The remaining beam proceeds to a silicon photomultiplier (SiPM), which serves as a reference for the measurement, to ensure the stability of the laser light.

At the first PMT position the laser beam has an intensity equal to the intensity of the transmitted beam of beamsplitter BS010, therefore $I_1 = 0.47$. At the second PMT position the beam has an intensity equal to the reflected beam of beamsplitter BS010 times the intensity of the reflected beam of beamsplitter BS049, thus $I_2 = 0.43 \cdot 0.28 = 0.12$. The adapted equation 4.6 for this setup is

$$U = \frac{E_\mathrm{L} \cdot QE \cdot T_\mathrm{D} \cdot T_\mathrm{F} \cdot I \cdot q_\mathrm{e} \cdot G \cdot 2 \cdot R}{E_\gamma \cdot t} \qquad (5.3)$$

where I is replaced by I_1 or I_2, depending on the position of the PMT.

5.4 Setup 3

This setup is used to measure the anode uniformity. For this a laser diode is used instead of the PiLas laser. The light of the laser diode is fed into an optical fibre, the other end of which is fixed to the motorised positioning table, which is movable along two axes. This way the laser beam can be moved, as to enter the PMT on different positions of the photocathode. Hence, the relation between the position at which the light enters the PMT and the height of the output signal can be determined.

The setup is shown in figure 17. It consists of the laser diode connected to one end of the optical fibre, the other end of which is connected to the ED1-C20-MD 20° circle tophat engineered diffuser and fixed to the motorised positioning table. The laser light passes from the diode through the fibre and diffuser before reaching the PMT. The PMT has to be positioned as close as possible to the fibre so that the beam spot remains small, with a diameter of roughly 5 mm, as its size increases with distance. A filter is not needed in this setup, since the light of the laser diode is much weaker than that of the PiLas laser.

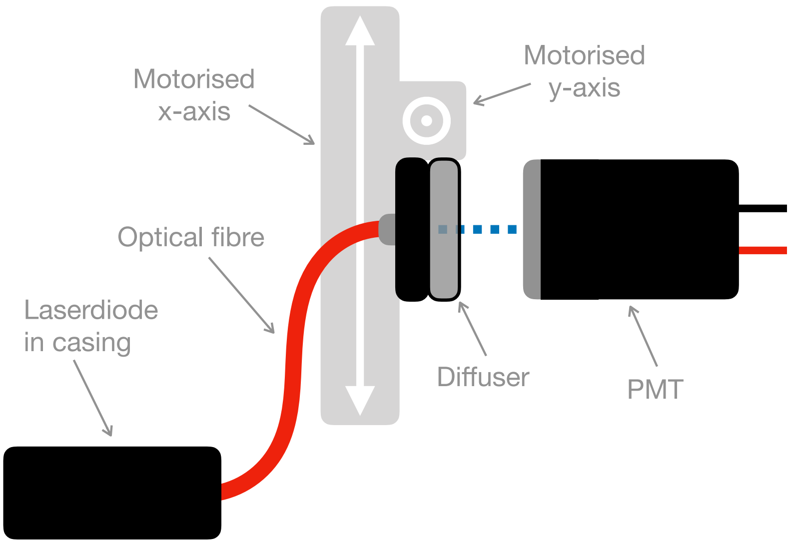

Figure 17: Setup 3 consists of a laser diode, an optical fibre, a ED1-C20-MD 20° circle tophat engineered diffuser, a positioning table with two motorised axes, and the PMT which is to be measured.

6 Measurements and Results

6.1 Anode Pulse Rise Time

The anode pulse rise time is the time it takes for the pulse to grow from 10% to 90% of the final pulse height, and thus gives information on the rapidity of the signal, as stated in [11], *page 250*. For the determination of the pulse height, the signal of each PMT is recorded ten times. For this measurement setup 1 is used, which is described in chapter 5.2, and where two PMTs are measured at the same time. The fact that the PMTs get an unequal amount of the laser light does not matter for this measurement.

The PMT signals are plotted and a linear fit is performed in the region of 10% to 90% of the signal amplitude. This can be seen in figure 18. The slope k and maximum amplitude A_{max} of this fit are thereby obtained as fit parameters and used to calculate the rise time t_{r} via

$$t_{\mathrm{r}} = \frac{0.9 \cdot A_{\mathrm{max}} - 0.1 \cdot A_{\mathrm{max}}}{k} = \frac{0.8 \cdot A_{\mathrm{max}}}{k} \tag{6.1}$$

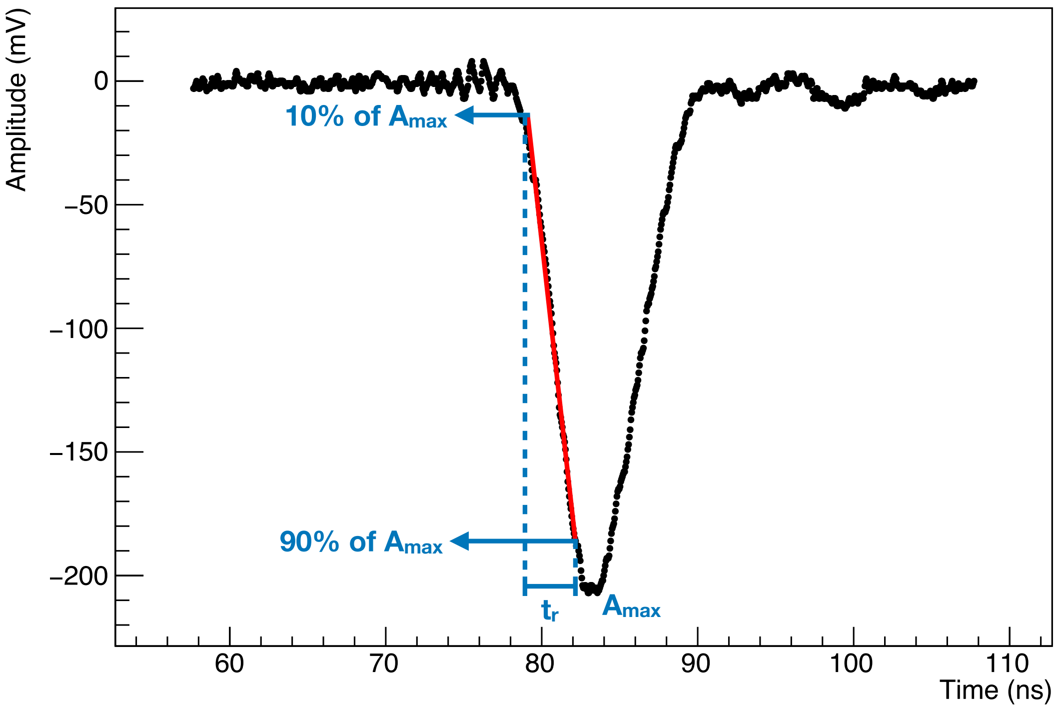

Figure 18: The laser signal measured with PMT RA2888 at a tune value of 60%, frequency of 200 Hz and applied voltage of 1150 V. The linear fit (red) from 10% to 90% of the negative edge of the pulse gives information on the anode pulse rise time t_{r}.

As the PMT signals fluctuate slightly, the final value of the anode pulse rise time of a PMT is the mean of ten plotted and fitted measurements. Table 6 shows these mean anode pulse rise times with standard deviation σ for the PMTs for three different applied voltages. The noise on the signal can sometimes be problematic for the fit. As this is the case especially for smaller signals, where the noise plays a bigger role, the measurements done with an applied voltage of 1050 V are fitted in a range between 15 % and 90 %. These values are marked with (1). A few of the measurements show a slightly bigger noise then the rest and are thus also fitted in a limited range, which is indicated by the raised indices.

	1050 V		1150 V		1250 V	
PMT Number	Rise Time (ns)	σ (ns)	Rise Time (ns)	σ (ns)	Rise Time (ns)	σ (ns)
RA2622	2.809 (1)	0.061	2.702	0.037	2.603	0.028
RA2632	2.850 (1)	0.017	2.743	0.014	2.606	0.011
RA2840	3.052 (1)	0.039	2.977	0.043	2.842	0.046
RA2843	3.282 (1)	0.081	3.044	0.056	2.967	0.049
RA2850	3.097 (2)	0.093	2.907 (1)	0.077	2.904	0.064
RA2880	3.042 (1)	0.049	2.979	0.078	2.904	0.046
RA2881	3.116 (1)	0.066	3.056	0.090	2.905	0.040
RA2884	3.014 (1)	0.017	3.038	0.019	2.866	0.016
RA2888	3.054 (1)	0.067	3.015	0.032	2.906	0.078
RA2889	2.907 (1)	0.108	2.898	0.024	2.794	0.056
RA2890	3.052 (1)	0.068	2.952	0.055	2.867	0.064
RA2891	3.049 (1)	0.027	3.078	0.079	3.011	0.066
RA2892	3.249 (6)	0.430	3.201 (2)	0.040	2.876 (1)	0.086
RA2903	3.046 (1)	0.030	3.041	0.022	2.926	0.042
RA2904	2.980 (1)	0.024	2.982	0.032	2.893	0.025
RA2908	3.193 (1)	0.059	3.112	0.055	2.978	0.051
RA2909	3.104 (1)	0.054	3.111	0.062	2.946	0.044
RA2910	3.165 (1)	0.058	3.037	0.047	2.969	0.049
RA2918	3.081 (1)	0.034	2.965	0.029	2.857	0.023
RA2922	3.183 (2)	0.046	3.120	0.031	2.997	0.040
RA2923	3.144 (1)	0.023	3.011	0.025	2.895	0.023
RA2924	2.962 (1)	0.035	2.925	0.046	2.825	0.070
RA2925	3.129 (1)	0.040	3.000	0.021	2.880	0.025
RA2926	3.002 (1)	0.070	3.017	0.071	2.885	0.033
RA2927	3.044 (2)	0.061	3.039	0.063	2.945	0.104
RA2928	3.192 (1)	0.071	3.104	0.107	2.948	0.133
RA2929	2.971 (3)	0.145	2.953 (1)	0.083	2.899	0.129
RA2932	3.008 (1)	0.033	2.964	0.033	2.848	0.021
RA2934	2.994 (1)	0.035	2.938	0.083	2.828	0.068
RA2937	3.236 (1)	0.105	3.016	0.022	2.932	0.035
RA2938	2.952 (1)	0.048	2.914	0.079	2.880	0.093
RA2940	3.066 (1)	0.059	2.907	0.038	2.845	0.023
RA2958	2.975 (1)	0.013	2.951	0.017	2.820	0.035
RA2960	3.322 (2)	0.129	2.956	0.020	2.973	0.015
RA2961	3.022 (1)	0.044	2.954	0.022	2.800	0.033

RA2962	3.010 (1)	0.038	3.062	0.041	2.912	0.046
RA2965	3.315 (3)	0.116	2.952 (1)	0.122	2.810	0.047
RA2968	3.787 (5)	0.224	3.204 (4)	0.098	3.064	0.120
RA2972	3.123 (1)	0.024	2.980	0.021	2.934	0.033
RA2976	3.132 (3)	0.147	3.129 (1)	0.081	2.894	0.133
RA2987	3.090 (1)	0.035	2.948	0.045	2.899	0.040
RA2988	2.982 (1)	0.075	2.977	0.039	2.869	0.029
RA2995	3.216 (4)	0.208	3.062 (1)	0.093	2.941	0.101
RA2996	3.072 (3)	0.157	2.890 (1)	0.105	2.950	0.118
RA3004	3.111 (1)	0.081	3.070	0.105	2.945	0.057
RA3006	3.106 (1)	0.083	2.963	0.052	2.913	0.054
RA3007	3.128 (1)	0.084	3.042	0.092	2.903	0.036
RA3010	2.969 (1)	0.061	2.935	0.039	2.818	0.032
ZU4328	3.119 (1)	0.030	3.048	0.026	2.909	0.034
ZU4329	2.958 (1)	0.064	2.918	0.024	2.845	0.042
ZU4330	3.086 (1)	0.101	3.018	0.089	2.856	0.035
ZU4403	3.038 (1)	0.038	2.916	0.022	2.817	0.025
ZU4404	3.169 (1)	0.088	2.985	0.089	2.883	0.047
ZU4407	3.252 (2)	0.044	2.928 (1)	0.087	2.867	0.038

Table 6: The measured anode pulse rise time and corresponding standard deviation of the measured PMTs. The rise time is the mean of ten measurements, with a fit of the falling edge between 10% to 90%. Raised indices indicate a limited fit range: (1) 15% to 90%, (2) 20% to 90%, (3) 25% to 90%, (4) 30% to 90%, (5) 35% to 90%, (6) 40% to 95%.

The anode pulse rise time of the PMTs is expected to be smaller than 3.4 ns. As can be seen in table 6 all of the PMTs have an anode pulse rise time smaller than 3.4 ns and therefore operate as expected.

6.2 Determination of the Gain

To determine the gain of a PMT firstly the amplitude of its signal is measured over a period of ten minutes. The measured data points are then plotted and a gaussian fit is applied, which gives the maximum and full width half maximum (FWHM), as well as their uncertainties. Figure 19 shows this fitted plot for PMT RA2903. The errorbars show the statistical uncertainties of the datapoints.

This measurement is conducted with setup 1. As already described, two PMTs are measured at the same time in that setup, with the help of a BS010 beamsplitter. The fact that the two PMTs do not get the exact same laser beam intensity has to be taken into account here, as less light means smaller amplitude. Table 7 lists the amplitudes and FWHMs of the PMTs measured at position 1 ($I_{\mathrm{t}} = 0.47$). Table 8 lists the amplitudes and FWHMs of the PMTs measured at position 2 ($I_{\mathrm{r}} = 0.43$). The amplitudes of all PMTs have a maximal uncertainty of 0.02 %, while the FWHMs have a maximal uncertainty of 0.3 %.

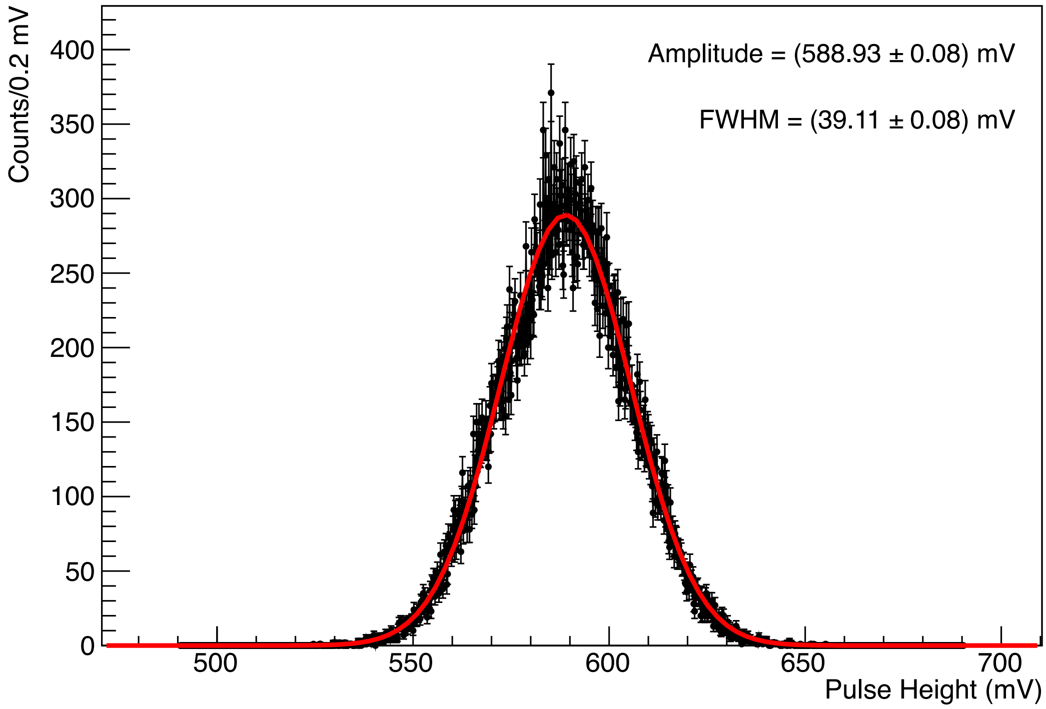

Figure 19: The laser signal measured by PMT RA2903 at position 1 with a laser tune value of 60%, frequency of 200 Hz and applied voltage of 1150 V. The red line is the gaussian fit, which gives the amplitude and FWHM, as well as their uncertainties.

	1050 V		1150 V		1250 V	
PMT Number	Amplitude (mV)	FWHM (mV)	Amplitude (mV)	FWHM (mV)	Amplitude (mV)	FWHM (mV)
RA2622	199	12	452	23	930	49
RA2632	225	11	496	28	1020	59
RA2840	151	10	328	19	680	39
RA2880	153	9	342	20	714	48
RA2881	130	8	294	20	627	41
RA2884	193	12	437	24	899	50
RA2889	162	11	358	25	731	49
RA2903	266	17	589	39	1185	77
RA2908	166	9	377	27	805	56
RA2910	158	11	357	24	735	49
RA2918	201	14	436	25	887	47
RA2923	158	10	256	23	744	46
RA2924	141	9	314	17	651	35
RA2926	140	9	307	19	620	37
RA2928	82	6	178	13	361	28
RA2932	240	14	527	34	1085	63

RA2934	115	6	257	15	521	31
RA2938	92	6	201	14	405	28
RA2958	188	12	415	26	851	51
RA2961	158	10	346	22	720	47
RA2965	85	5	181	12	362	26
RA2972	132	9	292	22	593	44
RA2987	185	11	408	26	821	50
RA2995	83	6	181	14	372	28
RA3004	145	9	313	18	640	38
RA3007	150	10	327	20	674	43
ZU4328	133	8	287	19	593	38
ZU4403	140	9	308	19	629	41

Table 7: The amplitude and FWHM of PMTs measured at position 1 ($I_t = 0.47$), for three different applied voltages. The measured amplitudes have a maximal uncertainty of 0.02 %, the FWHMs have a maximal uncertainty of 0.3 %.

	1050 V		1150 V		1250 V	
PMT Number	Amplitude (mV)	FWHM (mV)	Amplitude (mV)	FWHM (mV)	Amplitude (mV)	FWHM (mV)
RA2843	153	11	335	22	668	43
RA2850	129	8	286	19	568	38
RA2888	96	7	214	14	447	29
RA2890	110	7	246	16	511	32
RA2891	97	7	221	14	461	29
RA2892	100	7	219	14	452	28
RA2904	275	15	606	36	1246	76
RA2909	187	12	421	28	886	50
RA2922	116	7	254	16	525	32
RA2925	206	12	467	27	985	57
RA2927	117	7	256	15	514	33
RA2929	104	7	228	13	466	27
RA2937	144	9	311	19	643	40
RA2940	113	6	257	15	540	33
RA2960	278	16	596	35	1222	75
RA2962	105	7	226	14	457	28
RA2968	143	9	307	20	615	42
RA2976	76	5	167	11	348	24
RA2988	260	18	570	36	1119	73
RA2996	94	8	203	14	395	27
RA3006	168	11	364	24	717	47
RA3010	213	14	471 (*)	21	918 (*)	34
ZU4329	171	9	366	21	721	44

ZU4330	196	13	442	26	912	53
ZU4404	114	7	250	17	511	33
ZU4407	119	8	260	15	529	33

Table 8: The amplitude and FWHM of PMTs measured at position 2 (I_r = 0.43), for three applied voltages. The measured amplitudes have a maximal uncertainty of 0.02 %, the FWHMs have a maximal uncertainty of 0.3 %. $^{(*)}$ indicates limited fit range due to noise.

Given the signal amplitudes of the PMTs at a specific applied voltage, their corresponding gain can be calculated as shown in section 4.2. Equation 5.2 can be used to calculate the gain values of the PMTs in setup 1, using $I_t = 0.47$ for PMTs measured at position 1 (listed in table 7) and $I_r = 0.43$ for PMTs measured at position 2 (listed in table 8). Table 9 shows the calculated gain values, which have a maxmimal uncertainty of 7 %. As PMTs measured at position 1 get 47 % of the initial laser intensity, while PMTs measured at position 2 get only 43 %, their signal amplitudes cannot be directly compared. For this reason table 9 shows the amplitudes of all PMTs scaled up to correspond to 100 % initial laser intensity. These amplitudes have a maximal uncertainty of 5 %.

	1050 V		1150 V		1250 V	
PMT Number	Amplit. (mV)	Gain	Amplit. (mV)	Gain	Amplit. (mV)	Gain
RA2622	423	$6.82 \cdot 10^4$	962	$1.55 \cdot 10^5$	1979	$3.19 \cdot 10^5$
RA2632	479	$6.16 \cdot 10^4$	1055	$1.36 \cdot 10^5$	2170	$2.80 \cdot 10^5$
RA2840	321	$4.80 \cdot 10^4$	698	$1.04 \cdot 10^5$	1447	$2.16 \cdot 10^5$
RA2843	356	$5.84 \cdot 10^4$	779	$1.28 \cdot 10^5$	1553	$2.55 \cdot 10^5$
RA2850	300	$4.26 \cdot 10^4$	665	$9.44 \cdot 10^4$	1321	$1.87 \cdot 10^5$
RA2880	326	$4.69 \cdot 10^4$	728	$1.05 \cdot 10^5$	1519	$2.19 \cdot 10^5$
RA2881	277	$4.29 \cdot 10^4$	626	$9.70 \cdot 10^4$	1334	$2.07 \cdot 10^5$
RA2884	411	$5.64 \cdot 10^4$	930	$1.28 \cdot 10^5$	1913	$2.63 \cdot 10^5$
RA2888	223	$3.47 \cdot 10^4$	498	$7.71 \cdot 10^4$	1040	$1.61 \cdot 10^5$
RA2889	345	$5.77 \cdot 10^4$	762	$1.27 \cdot 10^5$	1555	$2.61 \cdot 10^5$
RA2890	256	$3.75 \cdot 10^4$	572	$8.40 \cdot 10^4$	1188	$1.75 \cdot 10^5$
RA2891	226	$3.85 \cdot 10^4$	514	$8.79 \cdot 10^4$	1072	$1.83 \cdot 10^5$
RA2892	233	$3.68 \cdot 10^4$	509	$8.05 \cdot 10^4$	1051	$1.66 \cdot 10^5$
RA2903	566	$8.04 \cdot 10^4$	1253	$1.78 \cdot 10^5$	2521	$3.58 \cdot 10^5$
RA2904	640	$8.93 \cdot 10^4$	1409	$1.97 \cdot 10^5$	2898	$4.04 \cdot 10^5$
RA2908	353	$5.19 \cdot 10^4$	802	$1.18 \cdot 10^5$	1713	$2.52 \cdot 10^5$
RA2909	435	$6.63 \cdot 10^4$	979	$1.49 \cdot 10^5$	2060	$3.14 \cdot 10^5$
RA2910	336	$5.03 \cdot 10^4$	760	$1.14 \cdot 10^5$	1564	$2.34 \cdot 10^5$
RA2918	428	$6.50 \cdot 10^4$	928	$1.41 \cdot 10^5$	1887	$2.87 \cdot 10^5$
RA2922	270	$4.43 \cdot 10^4$	591	$9.69 \cdot 10^4$	1221	$2.00 \cdot 10^5$
RA2923	336	$5.21 \cdot 10^4$	545	$8.45 \cdot 10^4$	1583	$2.45 \cdot 10^5$

RA2924	300	$4.93 \cdot 10^4$	668	$1.10 \cdot 10^5$	1385	$2.27 \cdot 10^5$
RA2925	479	$6.48 \cdot 10^4$	1086	$1.47 \cdot 10^5$	2291	$3.09 \cdot 10^5$
RA2926	298	$4.38 \cdot 10^4$	653	$9.59 \cdot 10^4$	1319	$1.94 \cdot 10^5$
RA2927	272	$4.15 \cdot 10^4$	595	$9.06 \cdot 10^4$	1195	$1.82 \cdot 10^5$
RA2928	174	$2.87 \cdot 10^4$	379	$6.21 \cdot 10^4$	768	$1.26 \cdot 10^5$
RA2929	242	$3.82 \cdot 10^4$	530	$8.38 \cdot 10^4$	1084	$1.71 \cdot 10^5$
RA2932	511	$7.36 \cdot 10^4$	1121	$1.62 \cdot 10^5$	2309	$3.33 \cdot 10^5$
RA2934	245	$3.41 \cdot 10^4$	547	$7.63 \cdot 10^4$	1109	$1.55 \cdot 10^5$
RA2937	335	$4.91 \cdot 10^4$	723	$1.06 \cdot 10^5$	1495	$2.20 \cdot 10^5$
RA2938	196	$2.98 \cdot 10^4$	428	$6.50 \cdot 10^4$	862	$1.31 \cdot 10^5$
RA2940	263	$3.43 \cdot 10^4$	598	$7.82 \cdot 10^4$	1256	$1.64 \cdot 10^5$
RA2958	400	$6.08 \cdot 10^4$	883	$1.34 \cdot 10^5$	1811	$2.76 \cdot 10^5$
RA2960	647	$1.02 \cdot 10^5$	1386	$2.19 \cdot 10^5$	2842	$4.49 \cdot 10^5$
RA2961	336	$5.41 \cdot 10^4$	736	$1.18 \cdot 10^5$	1532	$2.47 \cdot 10^5$
RA2962	244	$4.01 \cdot 10^4$	526	$8.63 \cdot 10^4$	1063	$1.74 \cdot 10^5$
RA2965	181	$3.02 \cdot 10^4$	385	$6.45 \cdot 10^4$	770	$1.29 \cdot 10^5$
RA2968	333	$5.56 \cdot 10^4$	714	$1.19 \cdot 10^5$	1430	$2.39 \cdot 10^5$
RA2972	281	$4.80 \cdot 10^4$	621	$1.06 \cdot 10^5$	1262	$2.16 \cdot 10^5$
RA2976	177	$2.96 \cdot 10^4$	388	$6.50 \cdot 10^4$	809	$1.36 \cdot 10^5$
RA2987	394	$6.73 \cdot 10^4$	868	$1.48 \cdot 10^5$	1747	$2.99 \cdot 10^5$
RA2988	605	$1.03 \cdot 10^5$	1326	$2.27 \cdot 10^5$	2602	$4.45 \cdot 10^5$
RA2995	177	$2.84 \cdot 10^4$	385	$6.20 \cdot 10^4$	791	$1.27 \cdot 10^5$
RA2996	219	$3.52 \cdot 10^4$	472	$7.60 \cdot 10^4$	919	$1.48 \cdot 10^5$
RA3004	309	$5.62 \cdot 10^4$	666	$1.21 \cdot 10^5$	1362	$2.48 \cdot 10^5$
RA3006	391	$6.41 \cdot 10^4$	847	$1.39 \cdot 10^5$	1667	$2.74 \cdot 10^5$
RA3007	319	$5.58 \cdot 10^4$	696	$1.21 \cdot 10^5$	1434	$2.50 \cdot 10^5$
RA3010	495	$7.40 \cdot 10^4$	1095	$1.64 \cdot 10^5$	2135	$3.19 \cdot 10^5$
ZU4328	283	$4.24 \cdot 10^4$	611	$8.98 \cdot 10^4$	1262	$1.89 \cdot 10^5$
ZU4329	398	$6.06 \cdot 10^4$	851	$1.30 \cdot 10^5$	1677	$2.55 \cdot 10^5$
ZU4330	456	$6.81 \cdot 10^4$	1028	$1.54 \cdot 10^5$	2121	$3.17 \cdot 10^5$
ZU4403	298	$4.90 \cdot 10^4$	655	$1.08 \cdot 10^5$	1338	$2.20 \cdot 10^5$
ZU4404	265	$4.44 \cdot 10^4$	581	$9.73 \cdot 10^4$	1188	$1.99 \cdot 10^5$
ZU4407	277	$4.46 \cdot 10^4$	605	$9.74 \cdot 10^4$	1230	$1.98 \cdot 10^5$

Table 9: Amplitude scaled up to laser intensity $I = 1$ and corresponding gain of all PMTs, for three different applied voltages. The gain values have a maximum uncertainty of 7 %, while the amplitudes have a maximal uncertainty of 5 %.

The gain of the PMTs should be $1 \cdot 10^5$ for an applied voltage lying between 1050 V and 1250 V, which is the case for all PMTs.

6.3 Electron Transit Time and Transit Time Spread

For the determination of the electron transit time (ETT), the time between the laser beam entering the PMT and the signal exiting the PMT has to be determined. For this the time delay between the laser trigger and the signal from the PMT is measured and the resulting data points plotted and fitted with a gaussian fit. The maximum of the fit gives the time delay, from which the electron transit time is calculated. The FWHM of the fit gives the transit time spread (TTS). A fitted plot of this measurement for one of the PMTs is shown in figure 20. The errorbars show the statistical uncertainties of the datapoints.

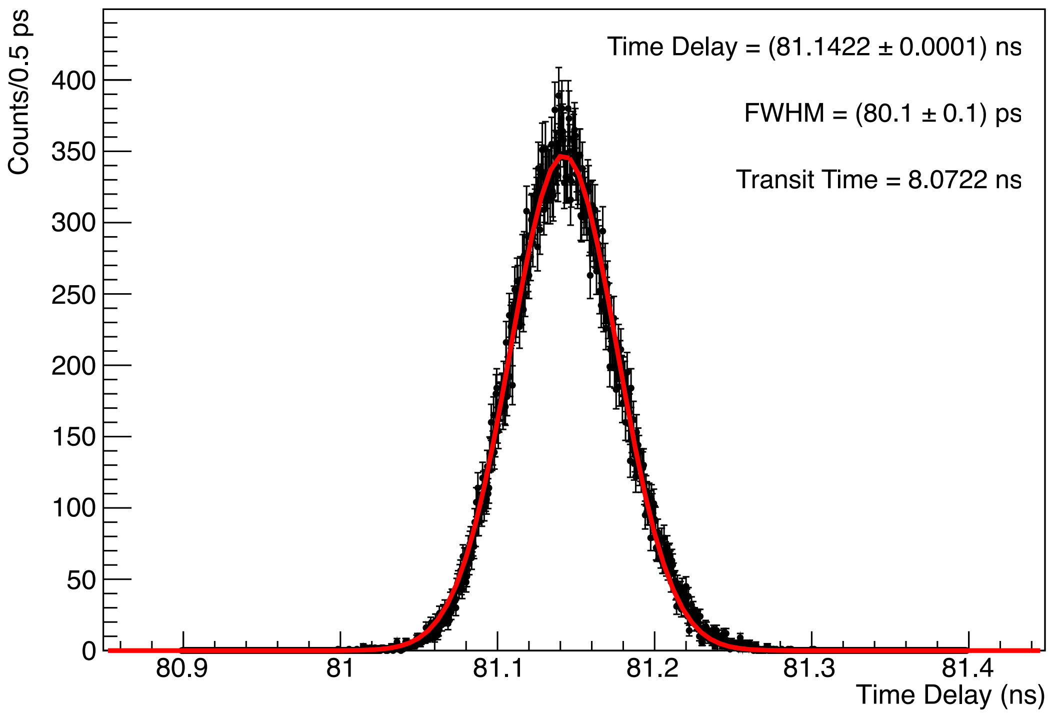

Figure 20: The time delay between trigger and signal measured with PMT RA2923 at position 1 with 60 % laser tune value, 200 Hz frequency and 1050 V applied voltage. The red line is the gaussian fit, the maximum gives the time delay (ETT + 73.07 ns), the FWHM gives the transit time spread.

This measurement is conducted with setup 1. As both PMT positions have the same distance to the laser, there is no difference between them for this measurement. However, as stated in [15] there is a delay of (73.07 ± 0.01) ns between the trigger and the optical signal of the laser, which has to be subtracted from the measured delay. Additionally, the length of the cables connecting the laser and PMT to the oscilloscope has to be taken into account. For measurements with setup 1 at SMI in Vienna the cables had the same length, compensating for an additional delay. However, for measurements with setup 1 at CERN the cables had different lengths, which is why for the PMTs measured there only (66.3 ± 0.1) ns where deducted from the measured value. These values are marked with $^{(c)}$.

The uncertainties of the measured delays given by the fit are below 0.001 ns for all PMTs. These are much smaller than the uncertainties of the delays stemming from the laser and cables. The uncertainties of the electron transit times measured at SMI are therefore below 0.015 %. The uncertainties of the electron transit times measured at CERN (indicated by $^{(c)}$) are below 0.151 %. The uncertainties of the transit time spreads given by the fits are below 5 %. The electron transit time and transit time spread of all PMTs are listed in table 10.

	1050 V		1150 V		1250 V	
PMT Number	ETT (ns)	TTS (ps)	ETT (ns)	TTS (ps)	ETT (ns)	TTS (ps)
RA2622$^{(c)}$	8.43	88	8.06	81	7.73	84
RA2632	9.46	57	9.20	43	8.87	56
RA2840$^{(c)}$	8.00	104	7.74	107	7.38	120
RA2843$^{(c)}$	8.23	128	7.94	100	7.60	121
RA2850$^{(c)}$	8.01	105	7.85	93	7.47	163
RA2880	7.98	62	7.44	56	7.16	69
RA2881	8.32	74	7.81	65	7.54	71
RA2884	8.16	62	7.64	55	7.35	59
RA2888	7.90	89	7.65	73	7.28	115
RA2889	7.85	51	7.44	84	7.09	65
RA2890	8.11$^{(*)}$	97	7.72	82	7.40	83
RA2891	8.09	89	7.61	90	7.34	89
RA2892	–	–	7.37	43	7.28	69
RA2903	8.04	79	7.61	84	7.28	77
RA2904	7.60	58	7.26	89	6.92	73
RA2908	7.93	73	7.48	157	7.12	97
RA2909	8.03	70	7.80	127	7.39	109
RA2910	8.10	67	7.79	168	7.35	107
RA2918	7.40	54	7.23	45	6.93	67
RA2922	7.83	88	7.62	105	7.29	95
RA2923	8.07	80	7.67	57	7.33	75
RA2924$^{(c)}$	7.97	125	7.60	101	7.26	121
RA2925	8.24$^{(*)}$	48	8.00	55	7.59	68
RA2926	7.58	103	7.34	112	6.99	123
RA2927	7.81	88	7.31$^{(*)}$	150	7.08	127
RA2928	7.32	100	7.13	136	6.73	209
RA2929	7.09	82	7.03	91	6.85	149
RA2932	7.49	77	7.12	75	6.78	91
RA2934	7.79	91	7.40	90	7.08	78
RA2937	7.96	59	7.65	68	7.29	89
RA2938	7.63	67	7.16	118	6.90	97
RA2940	8.08$^{(*)}$	64	7.66	114	7.34	74
RA2958	–	–	7.42	44	7.14	67

RA2960	–	–	7.57	99	7.24	51
RA2961	7.70	44	7.40	85	6.96	69
RA2962	7.98$^{(*)}$	59	7.31$^{(*)}$	56	7.18	73
RA2965	7.63	68	7.46	79	7.07	160
RA2968	8.08	64	7.48	60	7.34	65
RA2972	8.01	84	7.56	82	7.26	77
RA2976	8.20	81	7.51	67	7.38	90
RA2987$^{(c)}$	7.81	84	7.57	82	7.20	110
RA2988$^{(c)}$	8.19	101	7.87	85	7.47	82
RA2995$^{(c)}$	7.84	93	7.61$^{(*)}$	177	7.10	171
RA2996$^{(c)}$	7.51	94	7.40	111	7.14	165
RA3004$^{(c)}$	7.79	98	7.56	146	7.17	123
RA3006$^{(c)}$	8.02	134	7.63	126	7.32	102
RA3007$^{(c)}$	8.01	129	7.77	89	7.41	123
RA3010$^{(c)}$	7.85	124	7.52	83	7.22	95
ZU4328	7.84	65	7.63	52	7.29	102
ZU4329$^{(c)}$	8.10	89	7.71	97	7.35	105
ZU4330	7.89	91	7.64	62	7.19	62
ZU4403	7.74	57	7.51	60	7.09	84
ZU4404	7.77	72	7.28	68	7.03	76
ZU4407	7.37	48	7.29	57	7.04	96

Table 10: The electron transit time (ETT) and transit time spread (TTS) of the measured PMTs. Empty cells (–) indicate that the measurement could not be conducted because of interfering noise. $^{(*)}$ indicates fit in limited range. $^{(c)}$ indicates PMT tested at CERN.

The electron transit time of all PMTs lies below the expected value of 9.4 ns and the transit time spread of all PMTs lies below the expected value of 440 ps.

6.4 Stability over Time

The stability of the PMTs' performance over a longer period is again conducted with setup 1. However, the data acquisition here is automated with the help of a V785 32 Channel Multievent Peak Sensing ADC by CAEN (see [23]). It has a 4 V range which is divided into 4096 channels (12-bit resolution). The signal amplitudes of the PMTs are followingly measured in channels.

$$1 \text{ channel} = \frac{4000}{4096} \text{ mV} = 0.98 \text{ mV} \tag{6.2}$$

The PMT is measured for a few days. The data for each hour is then plotted as a histogram and a gaussian fit is applied. This way the average signal amplitude for each hour is attained as well as its uncertainty. These are then plotted, the resulting plot showing the average signal amplitude of each hour for the measured

PMT. From this the progression of the signal amplitude over time can be seen. Such a plot is shown in figure 21.

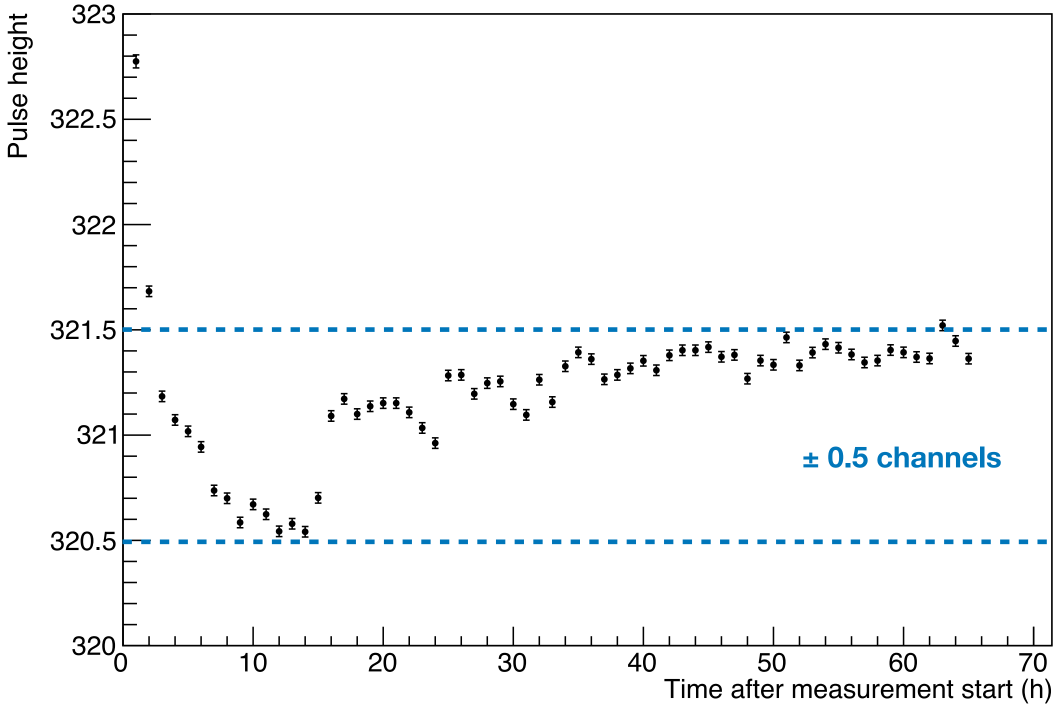

Figure 21: The progression of PMT RA2908's pulse height (given in channels) over a time of 65 hours, measured at a laser tune value of 50 %, frequency of 50 Hz, and 1050 V applied voltage.

One can clearly see that for a duration of 65 hours the signal amplitude of the PMT varies by only ±0.5 channels. The biggest disparities are at the beginning of the measurement. The first two data points have been taken out of the consideration as the PMT is still in its warm-up phase. However, even these two points only deviate by 2 channels from the average of the rest, which is less than 1 % of the signal amplitude. It can be concluded that the PMTs are stable over a period of several days.

6.5 Pulse Linearity

The measurement of the pulse linearity is done with setup 2 and is adapted from the measurement described by Hamamatsu ([12], *page 57-58*). For this two laser beams of different intensity are measured alternatingly by the PMT. Setup 2 provides a laser beam with intensity $I_1 = 0.47$ at position 1 and another laser beam with intensity $I_2 = 0.12$ at position 2. The measured PMT, which is fixed on the motorised positioning table, is moved back and forth between the two positions, taking alternating measurements of the two beams. The ratio of beam intensity I_1, at position 1, I_2, at position 2, has to be equal to the ratio of the corresponding PMT signal amplitude A_{01}, at position 1, and A_{02}, at position 2.

$$\frac{I_1}{I_2} = \frac{A_{01}}{A_{02}} \tag{6.3}$$

This measurement alternating between position 1 and position 2 is then repeated with higher beam intensities (higher tune value) of the laser. For sufficiently high beam intensities the output current of the PMT, and thus the measured amplitudes, A_1 and A_2, will deviate from linearity and equation 6.3 no longer holds. The percentage of deviation can be calculated as follows:

$$\left(\frac{A_1/A_2}{A_{01}/A_{02}} - 1\right) \cdot 100 \tag{6.4}$$

For fine mesh PMTs no deviation from linearity should be observed for anode currents under 300 mA ([12], *page 58*). Then the following holds:

$$\frac{A_1}{A_2} = \frac{A_{01}}{A_{02}} \tag{6.5}$$

	Position 1		Position 2	
	Amplitude (mV)	FWHM (mV)	Amplitude (mV)	FWHM (mV)
Measurement 1	204.42 ± 0.03	16.58 ± 0.03	51.23 ± 0.01	8.36 ± 0.01
Measurement 2	205.04 ± 0.03	16.43 ± 0.03	51.27 ± 0.01	8.32 ± 0.01
Measurement 3	206.05 ± 0.03	16.45 ± 0.03	51.47 ± 0.01	8.36 ± 0.01
Mean	205.17 ± 0.82	16.49 ± 0.08	51.32 ± 0.13	8.35 ± 0.02

Table 11: PMT RA2632 measured with a laser tune value of 10 %, a frequency of 100 Hz, and an applied voltage of 1150 V. The amplitudes and uncertainties are determined by a gaussian fit of the measurements. The mean is given with its standard deviation.

Table 11 shows the measurements for PMT RA2632 at a tune value of 10 %. This is the measurement with the lowest beam intensities, thus giving A_{01} and A_{02}, the mean amplitudes at positions 1 and 2. The ratio of amplitudes is:

$$\frac{A_{01}}{A_{02}} = 4.00 \pm 0.02$$

For the ratio of beam intensities, we have:

$$\frac{I_1}{I_2} = 3.92 \pm 0.26$$

Considering their given maximal uncertainties these two ratios are in agreement and equation 6.3 holds.

	Position 1		Position 2	
	Amplitude (mV)	FWHM (mV)	Amplitude (mV)	FWHM (mV)
Measurement 1	310.79 ± 0.05	20.46 ± 0.05	76.68 ± 0.02	10.38 ± 0.02
Measurement 2	311.81 ± 0.04	20.38 ± 0.05	77.01 ± 0.02	10.42 ± 0.02
Measurement 3	312.40 ± 0.04	20.16 ± 0.04	-	-
Mean	311.67 ± 0.81	20.33 ± 0.16	76.85 ± 0.23	10.40 ± 0.03

Table 12: PMT RA2632 measured with a laser tune value of 20 %, a frequency of 100 Hz, and an applied voltage of 1150 V. The amplitudes and uncertainties are determined by a gaussian fit of the measurements. The mean is given with its standard deviation.

Table 12 shows the measurements for PMT RA2632 at a tune value of 20 %. The ratio of A_1 and A_2, the mean values of the amplitudes measured at position 1 and 2, respectively, is:

$$\frac{A_1}{A_2} = 4.06 \pm 0.02$$

The deviation from A_{01}/A_{02} is therefore:

$$\left(\frac{4.06}{4.00} - 1\right) \cdot 100 = (1.50 \pm 1.02)\,\%$$

	Position 1		Position 2	
	Amplitude (mV)	FWHM (mV)	Amplitude (mV)	FWHM (mV)
Measurement 1	430.77 ± 0.05	22.69 ± 0.05	106.65 ± 0.02	11.97 ± 0.02
Measurement 2	431.92 ± 0.05	22.76 ± 0.05	106.80 ± 0.02	11.99 ± 0.02
Measurement 3	432.29 ± 0.05	22.84 ± 0.05	107.04 ± 0.02	12.03 ± 0.02
Mean	431.66 ± 0.79	22.76 ± 0.08	106.83 ± 0.20	12.00 ± 0.03

Table 13: PMT RA2632 measured with a laser tune value of 40 %, a frequency of 100 Hz, and an applied voltage of 1150 V. The amplitudes and uncertainties are determined by a gaussian fit of the measurements. The mean is given with its standard deviation.

Table 13 shows the measurements for PMT RA2632 at a tune value of 40 %. The ratio of A_1 and A_2, the mean values of the amplitudes measured at position 1 and 2, respectively, is:

$$\frac{A_1}{A_2} = 4.04 \pm 0.02$$

The deviation from A_{01}/A_{02} is therefore:

$$\left(\frac{4.04}{4.00} - 1\right) \cdot 100 = (1.01 \pm 1.00)\,\%$$

	Position 1		Position 2	
	Amplitude (mV)	FWHM (mV)	Amplitude (mV)	FWHM (mV)
Measurement 1	517.42 ± 0.06	27.02 ± 0.06	127.87 ± 0.03	14.08 ± 0.03
Measurement 2	517.26 ± 0.06	27.40 ± 0.06	127.59 ± 0.03	14.06 ± 0.03
Measurement 3	516.62 ± 0.06	27.31 ± 0.06	127.98 ± 0.03	14.31 ± 0.03
Mean	517.10 ± 0.42	27.24 ± 0.20	127.81 ± 0.20	14.15 ± 0.14

Table 14: PMT RA2632 measured with a laser tune value of 60 %, a frequency of 100 Hz, and an applied voltage of 1150 V. The amplitudes and uncertainties are determined by a gaussian fit of the measurements. The mean is given with its standard deviation.

Table 14 shows the measurements for PMT RA2632 at a tune value of 60 %. The ratio of A_1 and A_2, the mean values of the amplitudes measured at position 1 and 2, respectively, is:

$$\frac{A_1}{A_2} = 4.05 \pm 0.01$$

The deviation from A_{01}/A_{02} is therefore:

$$\left(\frac{4.05}{4.00} - 1\right) \cdot 100 = (1.25 \pm 0.76)\,\%$$

The values of the deviations in linearity for the different tune values are given with their maximum deviation. Considering these, it can be seen that the deviations in linearity are almost compatible with zero and thus linearity is given. This concurs with expectation as the highest currents observed in this measurement are under 10 mA.

6.6 Anode Uniformity

The anode uniformity is measured with setup 3, where the laser beam can be moved along two axes: left/right on the x-axis and up/down on the y-axis. That way, different points of the PMT's photocathode can be exposed to the laser light. For the measurement the beam is moved along these two axes of the motorised positioning table, stopping at different points, spaced 5 mm apart, for data taking. The measured points are positioned along four different lines: x-axis, y-axis, diagonal 1, and diagonal 2. They are shown in figure 22. At each point the signal amplitude of the PMT is measured for one minute, with an applied voltage of 1050 V for the PMT and a pulse width of 3.6 ns, frequency of 100 Hz, and voltage of 3.9 V for the laser diode.

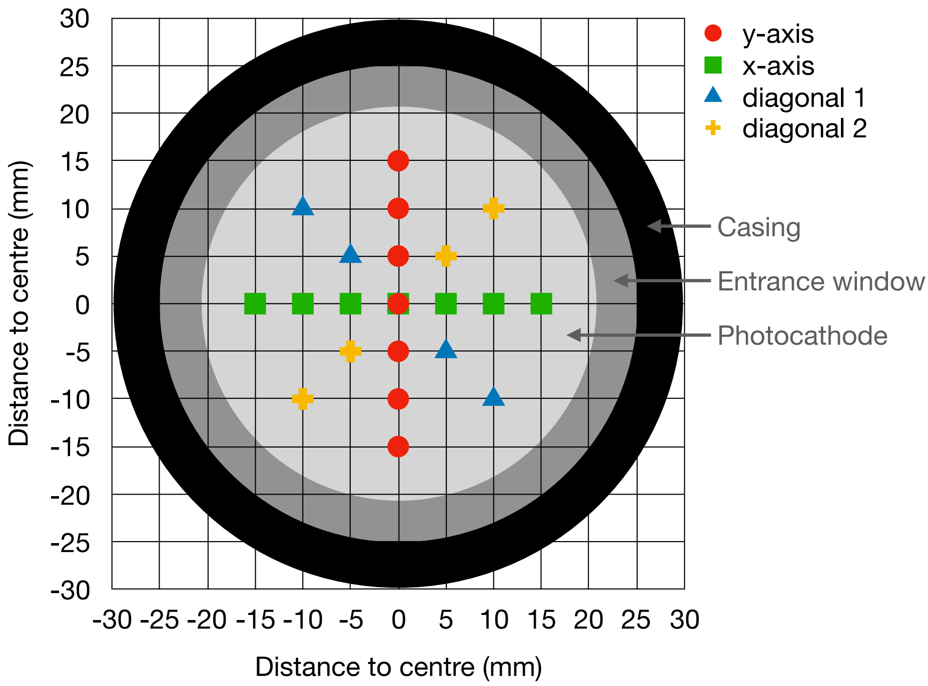

Figure 22: The measured points on the PMT's photocathode surface.

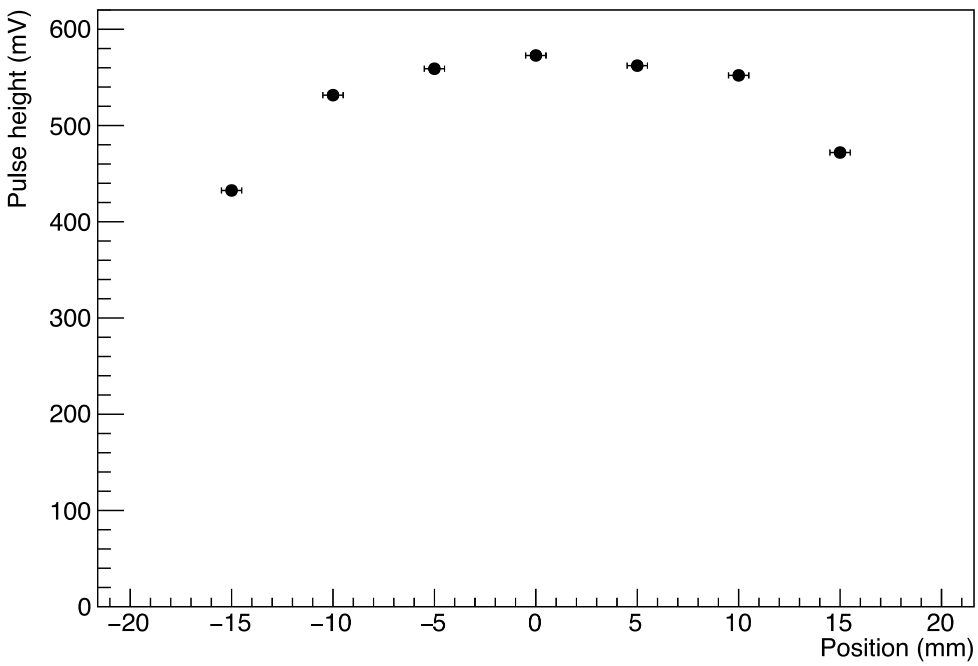

Figure 23: The amplitude of the signal measured in steps of 5 mm along the y-axis of the photocathode.

The photocathode has a diameter of 39 mm. Along the x- and y-axis, measurements are taken at seven different points, positioned −15 mm, −10 mm, −5 mm, 0 mm, 5 mm, 10 mm, and 15 mm away from the centre of the PMT. The resulting plots are shown in figure 23 and 24. The error bars in x-direction indicate the accuracy of the positioning, which is 1 mm. The error bars in y-direction show the uncertainties given by the fit of the pulse heights. They are below 1 % of the measured values and are therefore smaller than the filled circles representing the measured values.

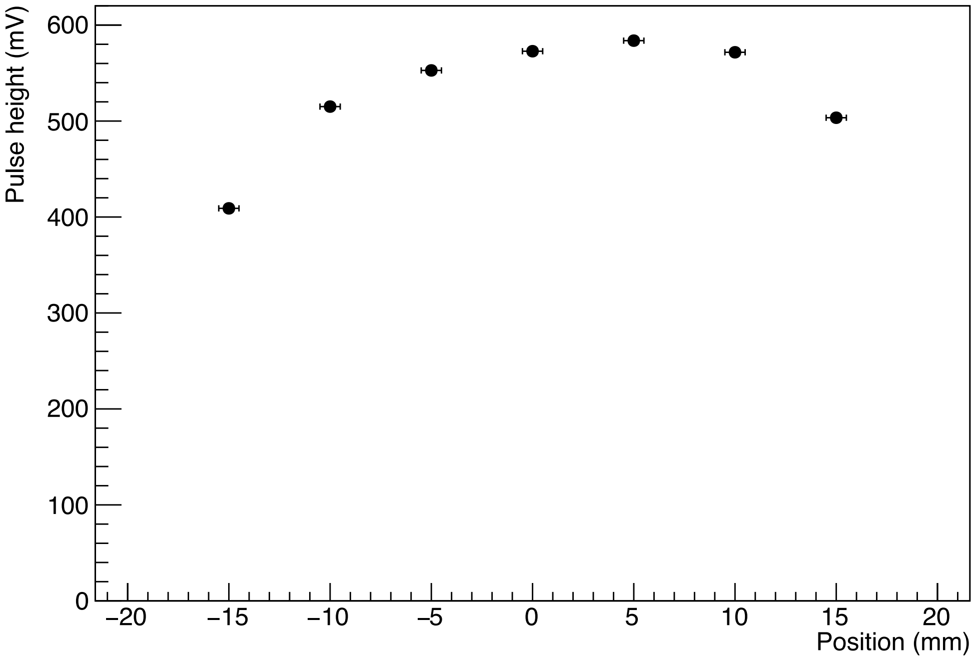

Figure 24: The amplitude of the signal measured in steps of 5 mm along the x-axis of the photocathode.

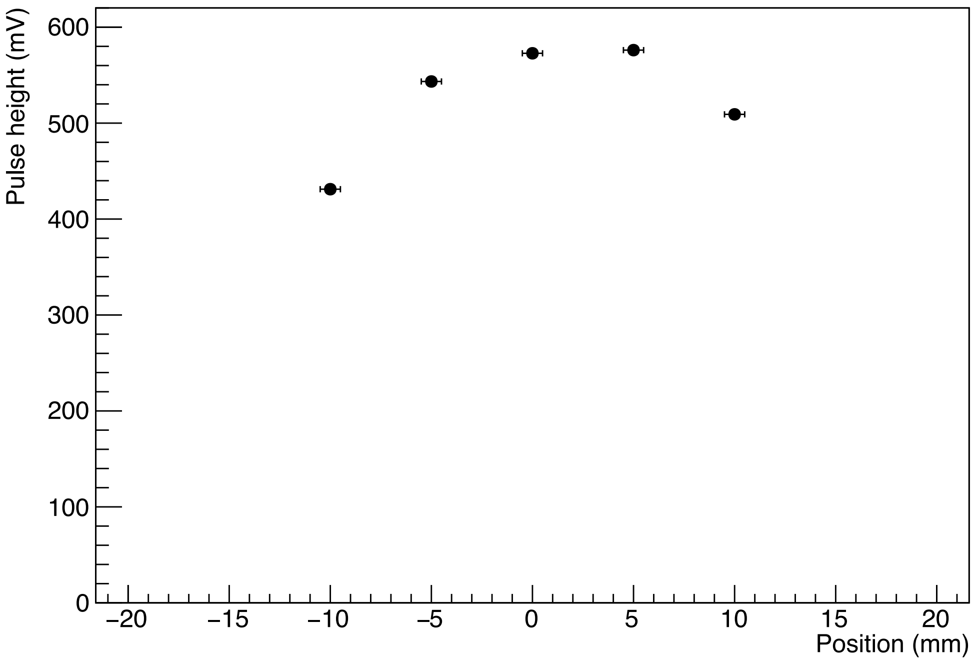

Figure 25: The amplitude of the signal measured in steps of 5 mm along diagonal 1 of the photocathode.

Along the x- and y-axis, measurements are taken at five different points, positioned −10 mm, −5 mm, 0 mm, 5 mm, and 10 mm away from the centre of the PMT. The resulting plots are shown in figure 25 and 26.

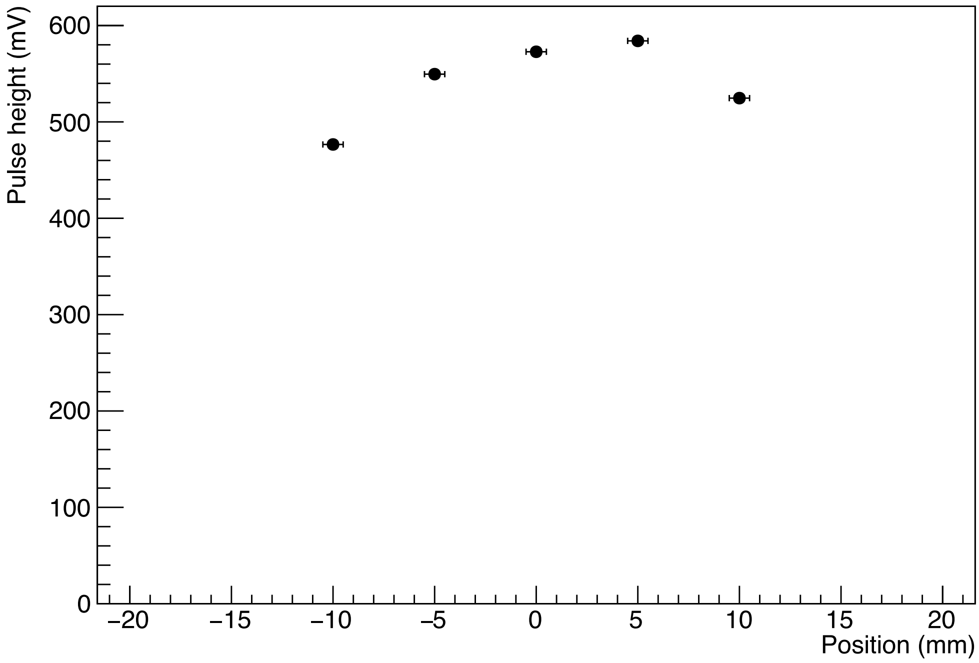

Figure 26: The amplitude of the signal measured in steps of 5 mm along diagonal 2 of the photocathode.

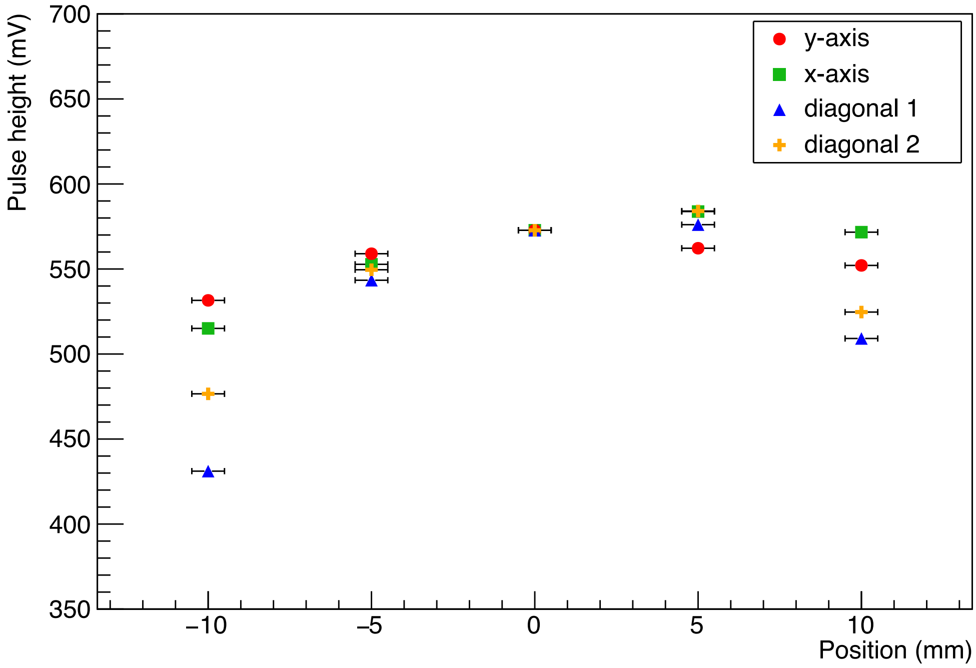

Figure 27: The amplitude of the signal measured in steps of 5 mm along the x-axis, y-axis, diagonal 1, and diagonal 2 of the photocathode.

For direct comparison of the four plots in figures 23 to 26, the measurements between −10 mm and 10 mm on all four axes for are combined in figure 27. It also shows the deviations in amplitude, with the measurement at the centre of the photocathode as reference. At a distance of 5 mm to the centre the amplitudes deviate by less than 5 %, while for a distance of 10 mm to the centre, the amplitudes deviate by up to 25 %.

For easier visualisation of these results, the combined data of the measurements along all four axes can be used to construct a three-dimensional plot of the amplitudes of the PMT signals, which is shown in figure 28. As there are only 23 data points (two additional data points on the y-axis and only one data point at 0 mm for all axes), the gaps have been filled in automatically by ROOT [24]. Hence, it has to be kept in mind, that amplitudes below 300 mV have not actually been measured.

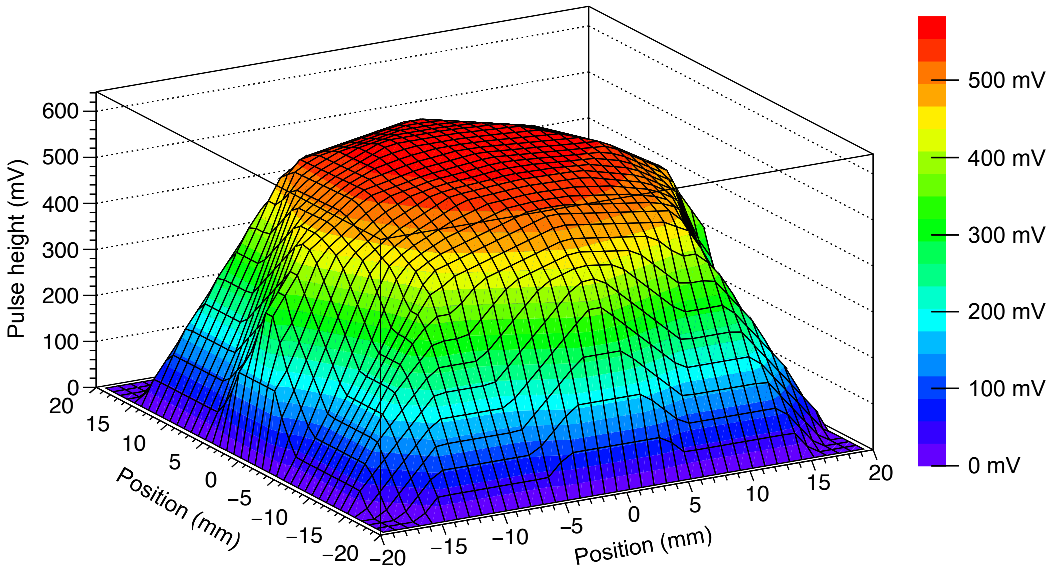

Figure 28: The amplitude of the signal generated by the laser on different positions of the PMT's photocathode. The positions are given as distance to the centre of the photocathode.

7 Conclusion

As part of the ALICE experiment's upgrade at CERN a new trigger system is installed. This Fast Interaction Trigger consists of two modules, the T0+ and the V0+, replacing the previous T0, V0, and FMD. The V0+ is a big scintillator ring, connected to fine mesh PMTs via optical fibres for readout. Before these PMTs are installed, they were thoroughly tested at SMI in Vienna and at CERN to ensure their optimal performance. For this three different setups where specifically designed to conduct measurements of six different characteristics.

The **anode pulse rise time** is the time it takes for the PMT's signal to increase from 10 % to 90 % of its full amplitude. It is expected to be under 3.4 ns for an applied voltage between 1050 V and 1250 V. The measurements show that this is the case for all PMTs, and that anode pulse rise time decreases with increasing applied voltage.

The **gain** of the PMTs is predicted to be $1 \cdot 10^5$ for an applied voltage between 1050 V and 1250 V. The gain is calculated from the measurements of the signal amplitude of the PMTs at applied voltages of 1050 V, 1150 V, and 1250 V. These calculations show that all PMTs have a gain of $1 \cdot 10^5$ between 1050 V and 1250 V applied voltage.

The **electron transit time** is the time it takes for the electrons to pass through the PMT while being multiplied by its dynodes (consisting of fine mesh in this case). This should be on average 9.4 ns. The measurements show that the electron transit time of the PMTs lies between 6.8 ns and 8.4 ns, which is below the given average. Followingly the PMTs have a good time resolution. The **transit time spread** is the variation in the electron transit time, given by the FWHM. It is expected to be averagely 440 ps. The measurements show that all PMTs have values between 10 % and 50 % of the given average. As the PMTs were always irradiated with a narrow laser beam, coming head-on, it is not surprising that the transit time spread is small.

To ensure the **stability** of the PMTs' performances measurements of the signal amplitude have been conducted for a duration of close to 70 hours. The evaluation shows that the amplitude is stable within 1 mV. The biggest changes in amplitude occur right at the beginning when the PMT is still warming up. However, even then the variation is under 2.5 mV for amplitudes around 315 mV.

The **pulse linearity** is determined by measuring the ratios of the signals generated by two beams of different intensities. For lower beam intensities the ratio of the signals should be equal to the ratio of beam intensities. By increasing the intensity of both beams the ratio of the two measured signals can start to deviate from the one at lower intensities. There should be no deviation under a current of 300 mA. This is the case for all PMTs. The observed deviations of under 2 % can be explained by uncertainties of the measurement itself.

The **anode uniformity** of the PMTs was measured by scanning the photocathode surface of the PMT with a laser, and measuring the signal amplitude at different off-centre positions. Up to 5 mm away from the centre the measured amplitudes deviate by under 5 %. For distances of 10 mm from the centre, the amplitudes deviate by up to 25 %.

As the PMTs all behave as expected they are ready to be installed in the V0+ module. The precise and detailed knowledge of their characteristics is essential for their exact placement within the V0+. This installation process already started in February 2020 at CERN. Due to the current situation and the consequent shutdown of CERN in March the installation of the remaining PMTs has meanwhile been postponed.

Abbreviations

ACORDE	ALICE Cosmic Ray Detector
ALICE	A Large Ion Collider Experiment
ALS	Advanced Laser Diode Systems
BAC	Basic Automation Component
CERN	European Organisation for Nuclear Research
EMCal	Electromagnetic Calorimeter
ETT	Electron Transit Time
FIT	Fast Interaction Trigger
FMD	Forward Multiplicity Detector
FWHM	Full Width Half Maximum
HMPID	High Momentum Particle Identification Detector
IP	Interaction Point
ITS	Inner Tracking system
LHC	Large Hadron Collider
LS2	Long Shutdown 2
MCH	Muon Chambers
MCP	Microchannel Plate
MTR	Muon Trigger
MWPC	Multi-wire Proportional Chambers
PHOS	Photon Spectrometer
PiLas	Picosecond Injection Laser
PMD	Photon Multiplicity Detector
PMT	Photomultiplier Tube
QCD	Quantum Chromodynamics
QGP	Quark-Gluon Plasma
SiPM	Silicon Photomultiplier
SDD	Silicon Drift Detectors

SMI Stefan Meyer Institute

SPD Silicon Pixel Detectors

SSD Silicon Strip Detectors

TOF Time of Flight

TPC Time Projection Chamber

TRD Transition Radiation Detector

TTS Transit Time Spread

ZDC Zero Degree Calorimeter

ZN Tungsten-quartz neutron calorimeter

ZP Brass-quartz proton calorimeter

List of Figures

List of Tables

References

[1] B. Abelev et al and The ALICE Collaboration. Upgrade of the ALICE experiment: Letter of intent. *J. Phys. G: Nucl. Part. Phys.*, 41(8):087001, 2014.

[2] CERN. What's in a name? `home.cern/about/who-we-are/our-history`. Accessed: Aug 10, 2020.

[3] CERN. The large hadron collider. `cds.cern.ch/record/1125888/files/bul-pho-2008-078.jpg`. Accessed: Aug 10, 2020.

[4] A. I. Maevskaya. Fast interaction trigger for the upgrade of the ALICE experiment at CERN: design and performance. *EPJ Web Conf.*, 204:11003, 2019.

[5] ALICE Collaboration. Performance of the ALICE experiment at the CERN LHC. *Int. J. Mod. Phys. A*, 29(24):1430044, 2014.

[6] R. Rapp, H. van Hees. Heavy quarks in the quark-gluon plasma. *Quark-Gluon Plasma 4*, page 111–206, 2010.

[7] C. Oppedisano. The ALICE zero degree calorimeter in pp physics. *Nuclear Physics B - Proceedings Supplements*, 215(1):173 – 175, 2011.

[8] CERN. A new schedule for the LHC and its successor. `home.cern/news/news/accelerators/new-schedule-lhc-and-its-successor`. Accessed: Apr 9, 2020.

[9] C. Y. Wong. *Introduction to High-Energy Heavy-Ion Collisions.* World Scientific, Singapore, 1994.

[10] W. H. Trzaska. New fast interaction trigger for ALICE. *Nuclear Instruments and Methods in Physics Research Section A*, 845:463 – 466, 2017.

[11] W. R. Leo. *Techniques for Nuclear and Particle Physics Experiments.* Springer-Verlag, Berlin Heidelberg, second edition, 1994.

[12] Hamamatsu Photonics K. K. *Photomultiplier Tubes: Basics and Applications*, third edition, 2006.

[13] Hamamatsu Photonics K. K. *Photomultiplier tube assembly H6614-70.* `www.hamamatsu.com/eu/en/product/type/H6614-70/index.html`. Accessed: May 22, 2020.

[14] Hamamatsu Photonics K. K. *Technical Information H6614-70-Y001*, Dec 2018.

[15] Advanced Laser Diode Systems A.L.S. GmbH. *PiLas Test Report (head: PIL040, mainframe: EIG1000D, serial number: 0307)*, third edition, Aug 2010.

[16] Advanced Laser Diode Systems A.L.S. GmbH. *Picosecond Injection Laser (PiLas): Owner's Manual*, third edition, Dec 2004.

[17] Thorlabs. *Mounted Absorptive Neutral Density Filters*. www.thorlabs.com/newgrouppage9.cfm?objectgroup_id=266. Accessed: Mar 23, 2020.

[18] Thorlabs. *NE30A transmission*. www.thorlabs.com/images/popupimages/NE30A.xlsx. Accessed: Mar 23, 2020.

[19] Thorlabs. *Engineered Diffusers*. www.thorlabs.com/newgrouppage9.cfm?objectgroup_id=1660. Accessed: Mar 23, 2020.

[20] Thorlabs. *Non-Polarizing Cube Beamsplitters (400-700 nm)*. www.thorlabs.com/newgrouppage9.cfm?objectgroup_id=754. Accessed: Mar 23, 2020.

[21] Thorlabs. *50:50 Non-Polarizing Beamsplitter Cube (400-700 nm)*. www.thorlabs.com/images/TabImages/NPBS_VIS_5050_RawData_E1.xlsx. Accessed: Mar 23, 2020.

[22] Thorlabs. *30:70 Non-Polarizing Beamsplitter Cube (400-700 nm)*. www.thorlabs.com/images/TabImages/NPBS_VIS_3070_RawData_E1.xlsx. Accessed: Mar 24, 2020.

[23] CAEN. *V785 32 Channel Multievent Peak Sensing ADC*. www.caen.it/products/v785/. Accessed: Aug 3, 2020.

[24] CERN. ROOT: Data analysis framework. root.cern.